Power System Protection and Control
ISSN:1674-3415

DESIGN AND CONTROL OF A FIRE HAWK OPTIMIZED 51-LEVEL ASYMMETRICAL MULTILEVEL INVERTER FOR IMPROVED STABILITY IN ISLANDED SINGLE-PHASE COMMUNITY MICROGRIDS

Sridevi A[1]*, H. R. Ramesh[2]

[*1]Research Scholar, Department of Electrical Engineering,
University Visvesvaraya College of Engineering,
K R Circle, Bangalore, Karnataka 560001, India.
[2]Professor & Chairman,
UVCE, K R Circle, Bangalore, Karnataka 560001, India.
*Email: sridevia712@gmail.com

Received:15 October 2025 **Revised**:18 November 2025 **Accepted**: 8 December 2025

***ABSTRACT*:**

This paper introduces a novel 51-level multi-level inverter (MLI) topology, addressing the challenge of minimizing component count in renewable energy systems. The proposed design features a hybrid asymmetrical configuration with reduced switches and Direct Current (DC)sources, enhancing efficiency and reducing complexity. To optimize power extraction from photovoltaic (PV) sources, a Walrus Optimized Recurrent Neural Network (WO-RNN) is employed, accurately predicting the maximum power point (MPP) under varying conditions. A Fire Hawks Optimization (FHO) based Cascaded Tilt Fractional Order Proportional Integral-Fractional Order Tilt Derivative (C-TFOPI-FOTD) controller governs the switching pulses of the MLI, ensuring precise voltage regulation and harmonic reduction. The proposed inverter control employs FHO due to its superior exploration exploitation balance and rapid convergence compared to conventional techniques such as PSO or GA. Simulation results confirm that FHO-optimized switching reduces THD and improves efficiency, validating its effectiveness for this system. In this work, a hybrid system integrates PV and wind power is used as input source. Simulation results, conducted in MATLAB/SIMULINK under an islanded single-phase microgrid with AC load, validate the effectiveness of the proposed system. The simulations demonstrate a low Total Harmonic Distortion (THD) of 1.29% for voltage and 1.78% for current, indicating high power quality. Furthermore, the proposed inverter topology achieves a high efficiency of 95.653%, attributed to reduce switching and conduction losses. These findings confirm the theoretical analysis and practical viability of the proposed 51-level MLI and its associated control strategies for the efficient integration of renewable energy sources into microgrid systems.

***Keywords**: Fire Hawks Optimization, Cascaded Tilt Fractional Order Proportional Integral-Fractional Order Tilt Derivative controller, Walrus Optimized Recurrent Neural Network, Multi-level inverter, solar PV.*

INTRODUCTION

With the ever-increasing need for electricity, the consumption of fossil fuels like coal and gas has skyrocketed in recent years [1]. These changes cause major issues and have a detrimental impact on the environment [2]. As a result, the electrical sector is seeing a rise in the usage of renewable energy sources (RES). Many studies have looked into the feasibility of generating power using RES[3]. Regardless of environmental concerns, all groups for power electronics and power system research agree that solar and wind power are the most popular RES[4]. The generation from solar and wind power systems varies with the weather.Furthermore, as an alternative energy generating technique, wind-based power generation is growing globally [5]. Seasonal fluctuations in the sources present a challenge to the use of solar and wind power generation. During winter, wind speeds typically rise, while solar irradiation often decreases[6]. The concept of hybridizing energy systems was developed in response to the increasing energy needs of the growing population. [7].

Many different Maximum power point tracking (MPPT) methods are used to maximize the power extraction from RES [8].A number of popular MPPT techniques have certain limitations; these include the Perturb and Observe (P&O), Incremental Conductance (INC), Open Circuit Voltage, and Short Circuit Current methods [9]. Therefore,

DOI: 10.46121/pspc.53.4.22

this paper proposed a novel MPPT method for obtaining a high range of power from sources. A power electronic device for converting direct current to alternating current is termed an inverter, which acts as an interface between DC sources and the grid [10]. The switching operation of the inverter is affected by the higher switching frequency and higher harmonics. Hence, necessary modifications are incorporated into the inverter designs [11]. In this regard, multi-level inverters are used in the power system to increase voltage levels. The multi-level inverter is widely adopted to outperform the two-level inverter in terms of output power quality while reducing switching losses, voltage stress, and filter needs [12]. Several authors suggested different control strategies to enhance the quality of output from the MLI. To improve MLI's THD, the author of [13] suggested a tweaked absolute sinusoidal pulse width modulation method. Honey badger with reptile search optimization algorithm was suggested in [14] for grid connected PV applications. Sliding mode control with an Adaptive Neuro-Fuzzy Inference Strategy was suggested by the author in [15] to control the cascaded H-bridge (CHB)MLI. Several methods are utilized to enhance the performance of MLI with fewer harmonics and errors.

As part of the suggested topology, the system uses a unique approach to inverter control: the C-TFOPI-FOTD controller. In [32],it is used to control the MPPT using the proportional integral (PI)controller. In [33], the DC motor is controlled by aproportional integral derivative (PID) controller that uses particle swarm optimization. Tilt Integral Derivative (TID)controllers are utilized in [34] for the transient lines' MPPT. Here, the FHO method is used to control the controller's gain parameters. Numerous researchers have developed various methods over time for regulating the controller's parameters. For the Static synchronous Compensator (STATCOM) renewable hybrid power system, a PI controller based on the whale optimization method was used [35]. Grey wolf optimization-based MPPT was used in [36] to regulate the settings of the innovative controller in wind and numerous other situations. In [40] single stage three phase differential fly back inverter (DFI) integrates voltage boosting DC-AC conversion and MPPT using conventional and modified INC techniques achieves high efficiency with improved tracking speed.In [41] suggests a modified firefly algorithm (MFA) and a multi-level adaptive model predictive control (MPC) framework to optimize hybrid microgrid operations achieving cost reduction, emission minimization, efficient power dispatch, and improved system stability.In [42] a double vector optimized MPC method for two-level inverters that reduces common mode voltage, THD and switching losses. In [43] presents a high gain soft switching DC-DC converter with a coupled inductor, single low resistance MOSFET MPPT algorithms for PV applications which achieves 95% efficiency.

MLI topologies are face difficulties by high switch counts, multiple DC sources, and rising circuit complexity, which make them unsuitable for scalability in medium and high-power applications. The majority of MPPT controllers experience slow convergence and are unable to track maximum power efficiently under rapidly varying irradiance.Inverters also face voltage stress, thermal losses, and decreased efficiency, particularly in large-scale renewable systems.To address these limitations, the work presented in this paper proposes a low-switch-count and low-DC-source-count compact inverter with a high-performance control scheme to achieve rapid MPPT convergence, efficiency enhancement, and power quality enhancement. To overcome the disadvantages in existing works, this paper proposed a novel controlling method. Among the various optimization algorithms reported in the literature like PSO, GA, FHO was selected for this study because it exhibits a strong capability to escape local minima, faster convergence rate, and robustness in managing nonlinear, high-dimensional optimization tasks. These features make FHO highly suitable for optimizing the switching angles of a multi-level inverter, where conventional techniques may require more iterations or yield sub-optimal solutions. The major objective of this paper is;

- To propose a novel 51-level MLI with fewer switches and DC sources for renewable energy connected power systems to improve efficiency.
- To accurate maximum power point prediction under varying PV conditions a Walrus optimized recurrent neutral network is used.
- A C-TFOPI-FOTD controller is designed to regulate switching pulses, improve voltage regulation and reduce harmonics and FHO is used to tune the gain parameters.

The remaining section of this paper is organized as follows: section 2 describes the MLI for various control strategies. In section 3, the proposed methodology explains the MLI inverter for enhancing the power quality. The results and discussion for validating the performance of MLI are described in section 4. Lastly, the conclusion part is described in section 5.

DOI: 10.46121/pspc.53.4.22

RELATED WORKS

Some of the existing works related to MLI with different control strategies are discussed in this section. Shivakumar et al. [16] suggested a novel MLI with 8 switches and 4 diodes. Grid connected PV with an MLI system was considered in this work. A space vector modulation technique was included in MLI to tune the switching pulses. This modulation method reduced the harmonics in the suggested inverter. The space vector modulation method performs better than a classical proportional-integral controller. Additionally, this modulation technique reduces the total harmonics in MLIs. A comparison between sinusoidal and space vector modulation in 51-level topology is conducted and this suggested system is tested and validated in MATLAB.Vijayvargiya et al. [17] recommended a new 51-level inverter and MPPT method for high power extraction. They optimized the INC to monitor the peak power of the solar PV. This MPPT method was improved by including the emperor penguin optimization algorithm with an INC method. The extracted peak power of the SPV is used by the buck converter to lower the voltage. Multi-level inverters are utilized to provide a lower harmonic voltage waveform in the output.A proportional resonant controller was used to control the MLI, and the Rain optimization algorithm was integrated with the controller for better output signal performance of the inverter. In order to reduce the number of switches, Thiyagarajan [18] anticipated a new 51-level MLI topology. The 12 switches in this MLI configuration were positioned in an asymmetrical fashion.The inverter can be made smaller and cheaper by reducing the number of switches. In order to attain the specified output levels, an inverter circuit's switching losses are defined by the number of conducting switches that must be used. The selective harmonic elimination pulse width modulation technique (SHEPWM) method is suggested in this study. The results are validated by changing the resistive and inductive loads.

Four asymmetrical DC voltage sources and fourteen switches were used to construct the suggested MLI by Law et al. [19]. A series-connected RL load was used to provide a linear load on which the switches were connected. Each separate asymmetrical DC voltage source in the suggested system has its own DC-DC buck converter, which can be either PV-battery or PV-non-battery based. Using the Nonlinear control technique (NLC) technique, the hybrid MLI was propelled. A voltage-controlled pulse width modulation (PWM) operating at 20 kHz was used to power each buck converter. A PID controller governs the DC-DC buck converter and the hybrid MLI is powered by the NLC technique to produce 51-level AC output voltage waveform.Jefry et al. [20] suggested a novel MLI with 14 switches, 4 diodes, and 5 DC sources. The quality of the generated output was enhanced by the 51-level MLI. An almost sinusoidal 51-level output voltage may be produced by the suggested MLI. When simulating optimal modulation, the THDwas less than the IEEE norm for applications below 69 kV. MATLAB/Simulink was used to verify the operation of the power factor correction STATCOM application. With fewer components the suggested MLI has produced high output voltage levels and great output quality.

Al-Samawi et al. [37] developed a minimum number of switches for PV systems in a nine-level cascade multi-level inverter. The recommended inverter exhibits a unity power factor and a decreased output voltage THD. The proposed system consists of reducing the partial shading condition (PSC). A comparison with the cascaded multi-level inverter (CMLI) topology was done in order to evaluate the performance of the suggested inverter. In order to provide a thorough performance benchmark, the assessment concentrated on modern cascade topologies that use the same nine voltage levels. The obtained topology is fed in MATLAB/Simulink, and the expected result is obtained in the system. Hassan et al. [38] established a reduced number of components with voltage boosting properties for a multi-cell 21-level hybrid multi-level inverter synthesizes. In order to create an output voltage waveform with 21 levels based solely on two uneven DC sources, the suggested system employs a hybrid 21-Level multi-level inverter, which includes two units: an H-bridge and a modified K-type unit. The suggested topology is simulated using the simulation system, and the controller is used to support the system. Additionally, it prolongs the life of the switching devices and lessens the voltage load on them. Additionally, fewer parts contribute significantly to cost and size savings.Sarebanzadeh et al. [39] distinguished a reducing the switches in the multi-level inverter topology for renewable energy sources. The suggested system consists of 25-level multi-level inverters for the renewable energy source, with the help of a PI controller to control the modulation technique of the fundamental frequency modulation. Large-scale multi-level inverters' ideal topologies are created with a number of goals in mind, such as minimizing the overall standing voltage for increased efficiency and dependability, increasing the number of output voltage levels, and minimizing the number of components (such as gate drivers and DC sources). The comparison of different methodsis shown in Table 1.

DOI: 10.46121/pspc.53.4.22

Power System Protection and Control
ISSN:1674-3415

Table 1: Comparative analysis of different methods

Author	Level	Number of switches	Number of sources	Modulation techniques	Type of MLI topology	Techniques	THD	Advantages	Disadvantages
Shivakumar et al. [16]	51	8	2	SVM	Asymmetrical MLI	-	2.82 %	THD was reduced	The loss was not considered.
Vijayvargiya et al. [17]	51	14	5	PWM	CHB	PR-ROA	-	Obtained maximum power from solar.	Harmonics are high
Thiyagarajan [18]	51	12	4	SHEPWM	Asymmetrical	PI	1.59 %	Harmonics was reduced.	High loss
Law et al. [19]	51	14	5	Unity	Isolated asymmetrical	PID	1.63 %	Extracted high power from sources	Load demand was not optimally satisfied.
Jefry et al. [20]	51	14	5	PWM	CHB	PI	3.19 %	Power quality was improved	The loss was high.
Al-Samawi et al. [37]	9	7	4	Phase disposition PWM	CMLI	PI	12.6 %	Lower Switching Losses	Potential DC Voltage Imbalance
Hassan et al. [38]	21	14	2	PWM	H bridge is cascaded with modified K-type unit	-	3.93 %	Lower Voltage Stress on Switches.	Challenges in Cascading for Large-Scale Implementation
Sarebanzadeh et al. [39]	25	10	2	PWM	Asymmetrical and cascaded mode	PI	3.85 %	Harmonics was reduced	High computational cost.
Proposed	51	10	4	PWM	Asymmetrical MLI	FHO-C-TFOPI-FOTD	1.29 %	Faster convergence and less harmonic reduction	Proposed work is not analyzed in grid connected mode

Recent advancements in MLI topologies, modulation strategies and controller optimizations, several gaps. Most works are essentially aimed at minimizing switches, optimizing modulating techniques (like SVM, SHEPWM, and PR controllers), or enhancing MPPT algorithms for integrating PVs. Moreover, certain MPPT controllers have poor convergence speed, rendering them unsuitable for tracking the MPP under high-rapidly changing irradiance. The use of optimization algorithms enhances control accuracy but introduces computational complexity that is unwanted in real-time implementation. Additionally, inverters, although very important in power conversion, are very heavily challenged in large and medium power systems by voltage stress, and lower efficiency. Adding more levels enhances the quality of the waveform but also adds higher circuit complexity, increased gate driver requirements, and more DC sources. Several topologies suggested in the literature remain suffer from by a large number of switching devices, which results in higher switching loss and thermal stress,

DOI: 10.46121/pspc.53.4.22

Power System Protection and Control
ISSN:1674-3415

ultimately degrading reliability. The majority of studies limit the performance analysis to ideal or steady-state conditions, ignoring resilience to nonlinear and actual disturbances. Thus, the evident research gap lies in realizing compact, economical, and experimentally proven inverter topologies with reduced switches and DC sources, aided by sophisticated control techniques that provide high efficiency, quick MPPT convergence, and better power quality for integration of renewable energy.

PROPOSED METHODOLOGY

Previous MLI topologies in solar PV power systems have needed a large number of switching components to generate the required output level. Hence, the power system suffers from switching losses and harmonics. In some topologies, a large number of DC sources were used, which increased the size of the inverter. One solution to this problem is a novel 51-level MLI that uses DC sources and has fewer switches for power systems that are connected to renewable sources. To provide input electricity, a hybrid system integrates PV and wind power. By utilizing the suggested WO-RNN, the maximum power that can be taken from the PV source is achieved. In order to enhance power quality, the proposed 51-level asymmetric multi-level inverter receives its input from the DC bus. The suggested inverter's switching pulse is controlled by an FHO optimized Cascaded Tilt fractional order proportional integral-fractional order Tilt Derivative (C-TFOPI-FOTD) controller.The FHO algorithm is then used to optimize the C-TFOPI-FOTD controller's gain setting to minimize error and harmonics.The performance of the proposed methodology is verified under an islanded single phase microgrid with AC load. Figure 1 represents the block diagram for the proposed work.

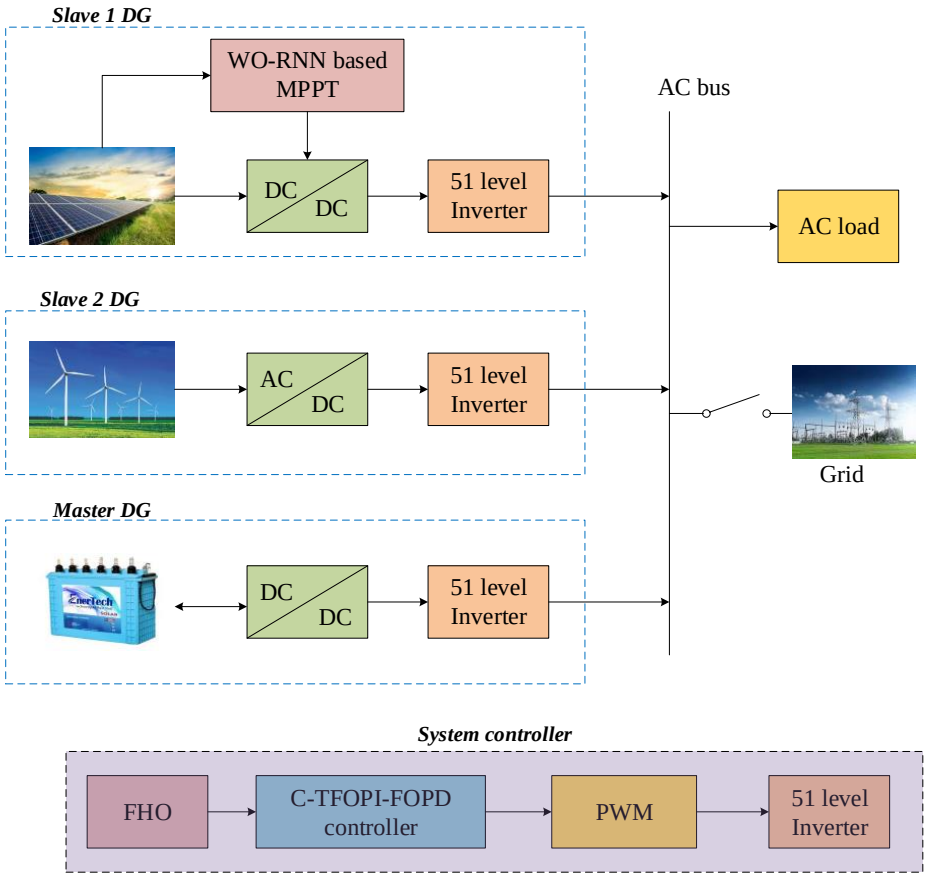

Figure 1: Block diagram for proposed work

The DC-DC Boost converter receives power from the PV system and sends it on to rectify the wind system's output using a diode bridge rectifier. A battery is used as an energy storage system to store surplus power supplied by various sources. The PV and wind are regarded as slave units, with the battery serving as the master unit. The output of these sources is fed to 51-level MLI. This MLI is controlled using the proposed control strategy and fed to an AC bus connected tothe load.

DOI: 10.46121/pspc.53.4.22

3.1. Modelling of solar PV

The PV effect is demonstrated by semiconductor materials used in PV cells, which are electronic devices that transform sunlight into electricity [21]. The PV cells are utilized to quantify the electric variables like resistance, voltage, and current, which vary with exposure to sunlight.Electron conduction happens when an electron in its bound state collides with other electrons, driven by the energy produced by the semiconductor's band gap. In the equivalent circuit of the PV modules, a diode, resistor, and light generating sources are all connected in parallel. The voltage-current (V-I) characteristics of the PV model used are expressed as:

$$\mathrm{I}_{\mathrm{Pv}} = \mathrm{I}_{\mathrm{Ph}} - \mathrm{I}_{S}\, e^{\left(\frac{q\left(V_{pv}+R_{s}\mathrm{I}_{\mathrm{Pv}}\right)}{\eta\kappa\mathrm{T}}-1\right)} - \frac{V_{\mathrm{Pv}} + R_{s}\mathrm{I}_{\mathrm{Pv}}}{R_{SH}} \tag{1}$$

From the above equation, the photo current is represented by I_{Ph}, the saturation current of the diode is denoted by I_{S}, the electron charge is indicated by q, the ideality factor of the P-N junction is N, and the temperature is denoted by T. The intrinsic shunt and series resistances of PV are represented by R_{SH} and R_{s}. In PV systems, DC-DC converters are frequently utilized to modify the PV voltage, whether stepping it up or down, while also playing a key role in maximizing power extraction via MPPT.Then, MPPT regulates the voltage and current of the PV module to maximize its output.

3.2 Walrus Optimized Recurrent Neural Network for MPPT

In this work, uncertainties in PV irradiance, temperature fluctuations, and converter non-linearities are addressed by the proposed WO-RNN based MPPT controller. RNN structure provides adaptive learning and dynamic mapping capability, enabling it to track the maximum power point even under rapidly varying conditions. Whale Optimization strategy ensures optimal parameter tuning, thus enhancing robustness against uncertainties compared to conventional deterministic MPPT methods. The duty cycle d is derived from a combination of the reference signal and voltage error, as expressed in the following equation [22].

$$v_{ER} = v_{\mathrm{MPP}(stc)} - v_{\mathrm{Pv}} \tag{2}$$

$$v_{\mathrm{Pv}} = v_{\mathrm{MPP}(stc)} + \gamma\left(\mathrm{T}_{REF} - \mathrm{T}\right) \tag{3}$$

Based on the temperature/voltage coefficient γ, the temperature gradient technique $v_{\mathrm{MPP}(stc)}$ adjusts using the PV module temperature T. The γ coefficient values depend on the type of module. The temperature based STC is represented by T_{REF}. A Recurrent Neural Network (RNN) is an advanced form of a traditional neural network designed specifically to handle sequential data [23]. An RNN maintains several features of a traditional neural network, such as neurons and connections. However, it is distinctive for its capability to process sequential inputs by using recurrent connections to repeat certain operations. This enables an RNN to maintain a memory of previously processed values, which can be utilized along with new inputs. For an input sequence, $\mathrm{I} = i_1, i_2, i_3, \ldots\ldots, i_{\mathrm{T}}$ the network executes the operation outlined in equation (4) at each step τ.

$$\begin{bmatrix} \hat{\rho}_{\tau} \\ k_{\tau} \end{bmatrix} = \varphi_{w}\left(i_{\tau}, k_{\tau-1}\right) \tag{4}$$

From the above equation, the hidden and output state is denoted by k_{τ} and $\hat{\rho}_{\tau}$. Additionally, φ_{w} denotes a neural network defined by a weight matrix W.The flexible structure of an RNN makes it well-suited for solving a variety of complex problems. The capacity of RNN architectures to maintain memory is improved by incorporating attention techniques. Performance in general and memory retention over lengthy sequences, in particular, are improved by this enhancement. Among the several attention implementations available, the Luong attention mechanism is employed in this study.

At each time step τ, the Luong attention mechanism computes encoded weights w_{τ} for an encoded source sequence, as described by equation (5).

DOI: 10.46121/pspc.53.4.22

$$\sum_{\delta} w_{\tau}(\delta)=1, \quad and \quad \forall \delta w_{\tau}(\delta)\geq 0 \tag{5}$$

The predicted output values at each time step are determined by a function that involves the RNN hidden state k_{τ}. This function also incorporates the weights assigned to the encoded hidden states, as outlined in equation (6).

$$\sum_{\delta} w_{\tau}(\delta) * \hat{k}_{\delta} \tag{6}$$

In the Luong attention model, sequence scores across the entire sequence are computed using the softmax function, as specified in the below equation;

$$w_{\tau}(\delta) \leftarrow \frac{Exp\left(\gamma_{\tau} * SCR\left(k_{\tau}, \hat{k}_{\delta}\right)\right)}{\sum_{\delta}\left(\gamma_{\tau} * SCR\left(k_{\tau}, \hat{k}_{\delta'}\right)\right.} \tag{7}$$

From the above equation, γ denotes the scaling parameter that controls the attention mechanism behaviors. Scores (SCR) for each sequence are defined by the dot product of each RNN hidden state k_{τ}, and the encoder hidden state $\hat{k}_{\delta}$, altered with the matrix W_{β} is expressed in the equation below;

$$SCR\left(k_{\tau}, \hat{k}_{\delta}\right) \leftarrow k_{\tau}^{\mathrm{T}} w_{\beta} \hat{k}_{\delta} \tag{8}$$

From the above equation, T denotes the extremeamount of repetitions.

The walrus optimization algorithm[24] is utilized in this study to select the optimal weight parameters. The population of walruses is mathematically represented using a population matrix. The walrus populations are initialized randomly, and the population matrix is computed and expressed as;

$$Y=\begin{bmatrix} Y_1 \\ \vdots \\ Y_j \\ \vdots \\ Y_{\mathrm{N}} \end{bmatrix}_{\mathrm{N}\times\mathrm{M}} = \begin{bmatrix} y_{1,1} & \cdots & y_{1,k} & \cdots & y_{1,\mathrm{M}} \\ \vdots & \ddots & \vdots & \iddots & \vdots \\ y_{j,1} & \cdots & y_{j,k} & \cdots & y_{j,\mathrm{M}} \\ \vdots & \iddots & \vdots & \ddots & \vdots \\ y_{\mathrm{N},1} & \cdots & y_{\mathrm{N},k} & \cdots & y_{\mathrm{N},\mathrm{M}} \end{bmatrix}_{\mathrm{N}\times\mathrm{M}} \tag{9}$$

From the above equation, the population of the walruses is denoted by Y, the candidate solution, and the total number of walruses is indicated by Y_j and N. The value of the k^{th} decision variable, as well as the total number of decision variables, are denoted by $y_{j,k}$ and M. During the exploration phase, the optimal position and corresponding weight value for the walruses are computed, and it is expressed as;

$$y_{j,k}^{\mathrm{P}_1} = y_{j,k} + R_{j,k}.\left(sw_k - \mathrm{I}_{j,k}.y_{j,k}\right) \tag{10}$$

$$Y_j = \begin{cases} \mathrm{Y}_j^{\mathrm{P}_1}, \mathrm{E}_j^{\mathrm{P}_1} < \mathrm{E}_j \\ \mathrm{Y}_j, \ else \end{cases} \tag{11}$$

where, updated weight value for j^{th} walrus in the 1st stage and its k^{th} dimension is represented by $Y_j^{\mathrm{P}_1}$ and $y_{j,k}^{\mathrm{P}_1}$, random number lies between 0 to 1 is denoted as $R_{j,k}$, strongest walrus with best weight parameter is indicated by SW and integers randomly selected from the interval 0 to 1 is indicated by $\mathrm{I}_{j,k}$. $\mathrm{E}_j^{\mathrm{P}_1}$ denotes the objective function.

In the migration phase, updated weight parameter is initially generated, and it enhances the objection function value, then it is expressed as;

$$y_{j,k}^{\mathrm{P}_2} = \begin{cases} y_{j,k} + R_{j,k}.\left(y_{l,k} - \mathrm{I}_{j,k}.y_{j,k}\right), & \mathrm{E}_l < \mathrm{E}_j \\ y_{j,k} + R_{j,k}.\left(y_{j,k} - y_{l,k}\right), & else \end{cases} \tag{12}$$

DOI: 10.46121/pspc.53.4.22

Power System Protection and Control
ISSN:1674-3415

$$Y_j = \begin{cases} Y_j^{P_2}, & E_j^{P_2} < E_j \\ Y_j, & else \end{cases} \quad (13)$$

From the above equation, updated weight value for j^{th} walrus in the second stage, along with its dimension, is denoted by $Y_j^{P_1}$ and $y_{j,k}^{P_1}$. $E_j^{P_2}$ denotes the objective function, $Y_l, l \in \{1,2,.....,N\}$ and $k \neq j$ it denotes the weight value ofselected walrus for migrating the j^{th} walrus, k^{th} dimension. Its updated objective value is indicated by $y_{l,k}$ and E_l.

In the exploitation phase, aupgraded weight parameter is randomly generated, and it is expressed as;

$$y_{j,k}^{P_3} = y_{j,k} + \left(LB_{L,k}^{\tau} - \left(UB_{L,k}^{\tau} - R \,.\, LB_{L,k}^{\tau}\right)\right) \quad (14)$$

$$Local\ bounds: \begin{cases} LB_{L,k}^{\tau} = \dfrac{LB_k}{\tau} \\ UB_{L,k}^{\tau} = \dfrac{UB_k}{\tau} \end{cases} \quad (15)$$

$$Y_j = \begin{cases} Y_j^{P_3}, & E_j^{P_3} < E_j \\ Y_j, & else \end{cases} \quad (16)$$

Based on the third stage, weight updated value for j^{th} walrus and its k^{th} dimension is denoted by $Y_j^{P_3}$ and $y_{j,k}^{P_3}$, the iteration counter and its objection function is represented by τ and $E_j^{P_3}$, and the upper bound and lower bound of j^{th} walrus are indicated by UB_k and LB_k where k^{th} variable is represented by $UB_{L,k}^{\tau}$ and $LB_{L,k}^{\tau}$.

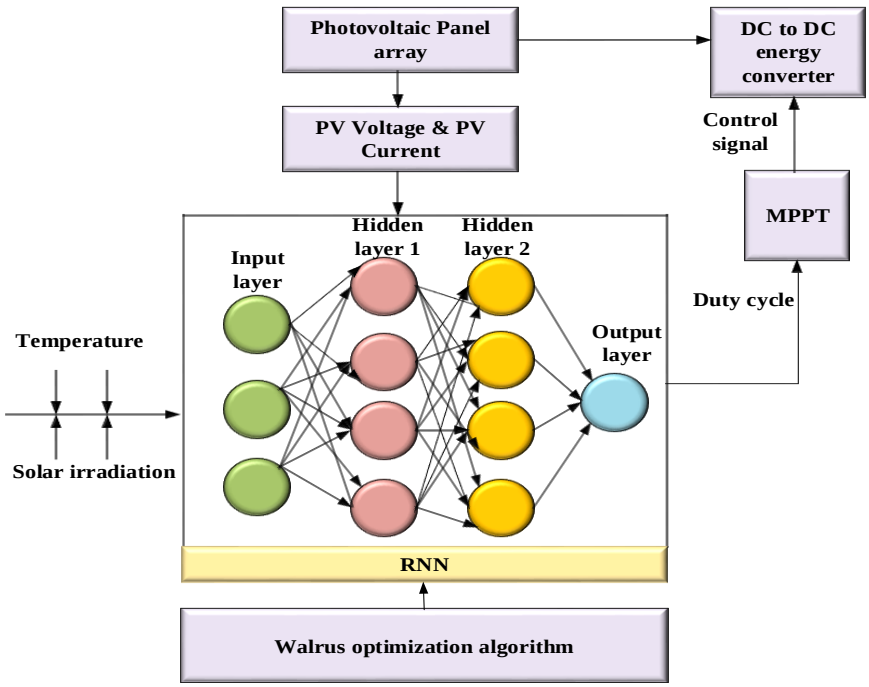

Figure 2:Block diagram for walrus optimized RNN based MPPT controller

DOI: 10.46121/pspc.53.4.22

Power System Protection and Control
ISSN:1674-3415

Figure 2 represent block diagram of the proposed walrus optimized RNN based MPPT scheme. PV panel outputs like voltage and current along with ambient temperature and solar irradiation provide inputs to RNN. RNN predicts maximum power point reference. The optimized duty cycle is then passed to the MPPT controller that drives the DC–DC converter to ensure maximum power extraction from PV system.

3.3 Modelling of Wind

Wind turbines play a crucial role in wind energy systems, serving as the primary movers for electric generators that they directly power through their shafts. The transformation of wind energy into kinetic energy is the process that produces mechanical energy [25]. The power generated by the wind turbine can be represented as;

$$P_M = 0.5 K_P(\beta,\gamma) A \rho v_\mu^3 \quad (17)$$

From the above equation, the swept area of the blades is denoted by A, the pitch angle of the blade is indicated by γ, the tip-speed ratio is denoted by β, air density, and the wind speed is denoted by ρ and v_μ. The turbine's performance coefficient is indicated by K_P.

3.4Proposed 51-level MLI

The proposed 51-level inverter with 10 switches and 4 voltage sources is shown in Figure 3.In the proposed inverter design, Insulated Gate Bipolar Transistors (IGBTs) are employed due to their high voltage blocking capability and fast switching characteristics. Each IGBT is selected to withstand at least 2–3 times the maximum expected blocking voltage per device to ensure safe operation. With the proposed 51-level MLI structure, IGBTs are subjected to a maximum stress of 120 V per switch, which is well below the selected device rating, thus guaranteeing reliable operation and reduced switching/conduction losses.In the suggested inverter design, the voltage sources for V1, V2, V3, and V4 were symmetrical in the ratio of 1:1:3:3, correspondingly. Additionally, the voltage sources are chosen in such a way that the output and load both have the step voltages that are intended. For V1, V2, V3, and V4, the selected values for the voltage sources are 30V, 30V, 90V, and 90V, respectively.Table 2 presents the 51 levels that were generated using the switching sequence in accordance with the recommended topology. In the tabular representation, the variables 0 and 1 denote the OFF states and ON switching states, respectively. The architecture under consideration yields a maximum voltage of 240 V and a minimum value of zero. Different modes of operations are investigated in Figure 3.

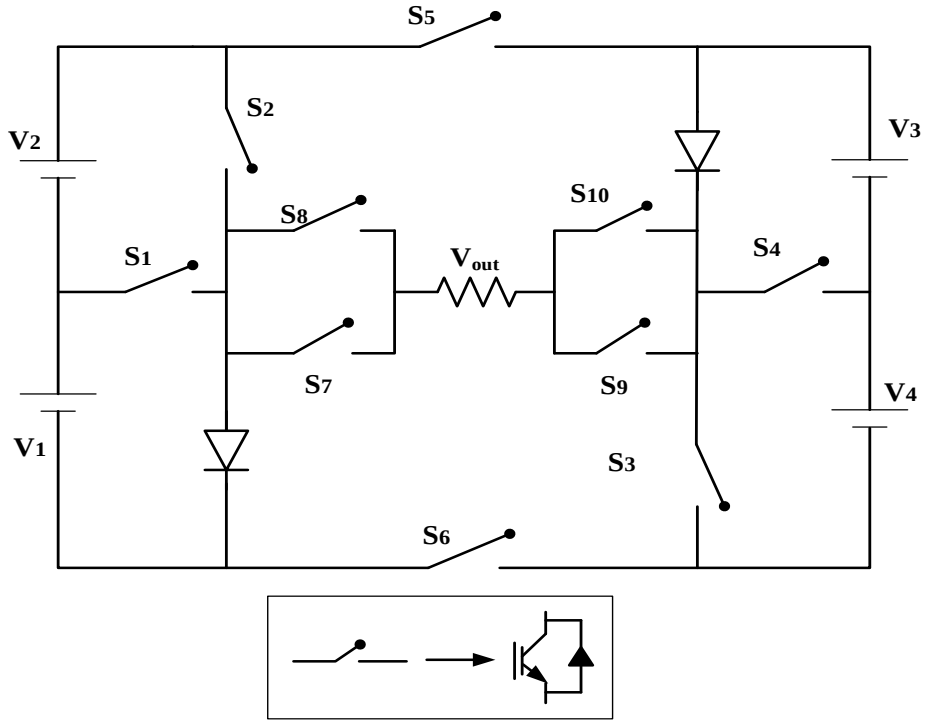

Figure 3: Proposed 51 level inverter

DOI: 10.46121/pspc.53.4.22

Power System Protection and Control
ISSN:1674-3415

PV array output voltage is first processed through a DC–DC converter stage, which is controlled by the WQ-RNN based MPPT to regulate the voltage at an optimal DC link level. This regulated DC voltage is then supplied to the 51-level inverter. Similarly, wind source after AC–DC conversion and the battery via a bidirectional DC–DC converter are also interfaced with individual 51-level inverters. This ensures that all DG units are properly linked to the AC bus.

Table 2: Switching pulses for the proposed 51-level inverter

Switches										
S1	**S2**	**S3**	**S4**	**S5**	**S6**	**S7**	**S8**	**S9**	**S10**	**V_{out}**
0	0	1	1	1	0	1	0	0	1	$25V_{dc}$
0	0	0	0	1	0	1	0	0	1	$24\ V_{dc}$
1	0	1	0	1	0	1	0	0	1	$23\ V_{dc}$
0	1	0	0	1	0	1	0	0	1	$22V_{dc}$
0	0	1	0	1	0	1	0	0	1	$21V_{dc}$
0	0	0	1	1	0	1	0	0	1	$20V_{dc}$
1	1	0	0	1	0	1	0	0	1	$19V_{dc}$
0	1	0	1	1	0	1	0	0	1	$18V_{dc}$
1	0	0	1	1	0	1	0	0	1	$17V_{dc}$
0	1	0	0	1	0	1	0	0	1	$16V_{dc}$
1	1	0	0	1	0	1	0	0	1	$15V_{dc}$
0	0	1	0	1	0	1	0	0	1	$14V_{dc}$
1	0	1	0	1	1	1	0	0	1	$13V_{dc}$
0	0	0	1	0	1	1	0	0	1	$12V_{dc}$
1	0	0	1	0	1	1	0	0	1	$11V_{dc}$
0	1	0	0	0	1	1	0	0	1	$10V_{dc}$
1	1	0	0	0	1	1	0	0	1	$9V_{dc}$
0	0	1	0	0	1	1	0	0	1	$8V_{dc}$
1	0	1	0	0	1	1	0	0	1	$7V_{dc}$
0	0	0	1	0	1	1	0	0	1	$6V_{dc}$
1	0	0	1	0	1	1	0	0	1	$5V_{dc}$
1	1	0	0	0	1	1	0	0	1	$4V_{dc}$
0	1	1	0	0	1	1	0	0	1	$3V_{dc}$
1	0	0	1	0	1	1	0	0	1	$2V_{dc}$
0	1	0	1	0	1	1	0	0	1	$1V_{dc}$
0	1	0	0	1	0	1	0	0	1	$0V_{dc}$
1	1	1	1	1	0	0	1	1	0	$-1V_{dc}$
0	1	0	1	1	0	0	1	1	0	$-2V_{dc}$
1	1	1	0	1	0	0	1	1	0	$-3V_{dc}$
1	1	0	1	1	0	0	1	1	0	$-4V_{dc}$
0	0	1	1	1	0	0	1	1	0	$-5V_{dc}$
1	0	1	0	1	0	0	1	1	0	$-6V_{dc}$
0	1	1	0	1	0	0	1	1	0	$-7V_{dc}$
1	0	1	1	1	0	0	1	1	0	$-8V_{dc}$
1	1	1	0	1	0	0	1	1	0	$-9V_{dc}$
1	0	1	1	1	0	0	1	1	0	$-10V_{dc}$
0	0	1	1	1	0	0	1	1	0	$-11V_{dc}$
0	1	0	1	1	0	0	1	1	0	$-12V_{dc}$
1	1	1	0	1	0	0	1	1	0	$-13V_{dc}$
0	1	1	0	0	1	0	**1**	**1**	0	$-14V_{dc}$
0	0	1	1	0	1	0	1	1	0	$-15V_{dc}$
1	1	0	0	0	1	0	1	1	0	$-16V_{dc}$
1	0	0	0	0	1	0	1	1	0	$-17V_{dc}$
0	1	0	0	0	1	0	1	1	0	$-18V_{dc}$
0	0	1	0	0	1	0	1	1	0	$-19V_{dc}$
0	0	0	1	0	1	0	1	1	0	$-20V_{dc}$

DOI: 10.46121/pspc.53.4.22

Power System Protection and Control
ISSN:1674-3415

0	1	1	1	0	1	0	1	1	0	$-21V_{dc}$
0	1	1	1	0	1	0	1	1	0	$-22V_{dc}$
0	1	1	1	0	1	0	1	1	0	$-23V_{dc}$
0	1	1	1	0	1	0	1	1	0	$-24V_{dc}$
1	0	0	1	0	1	0	1	1	0	$-25V_{dc}$

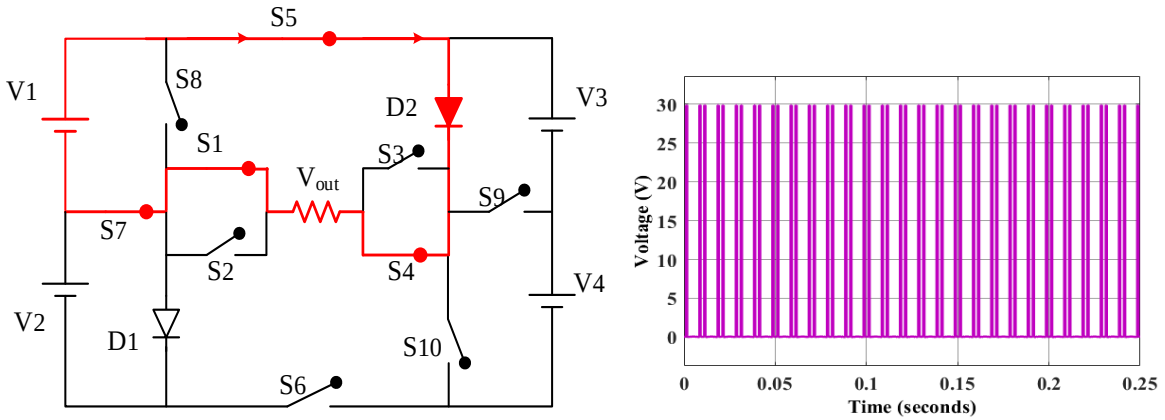

(a)

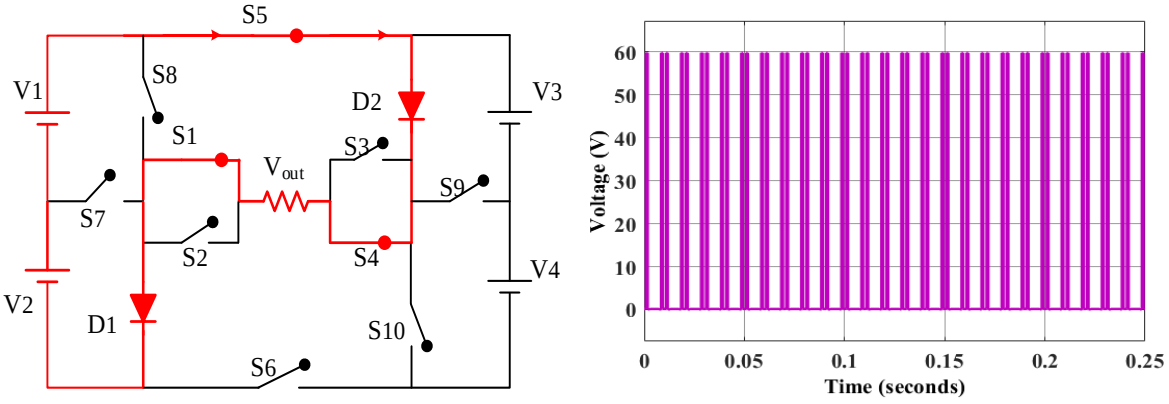

(b)

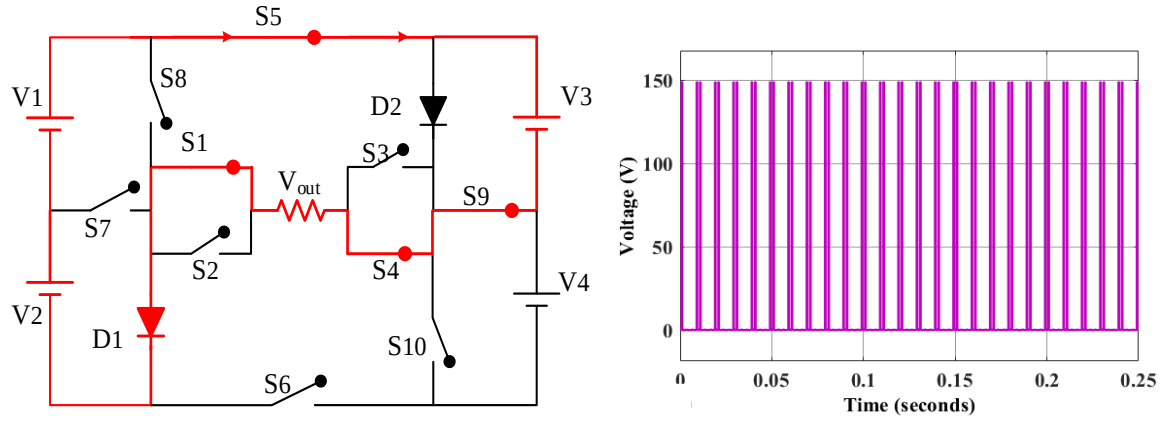

(c)

DOI: 10.46121/pspc.53.4.22

Power System Protection and Control
ISSN:1674-3415

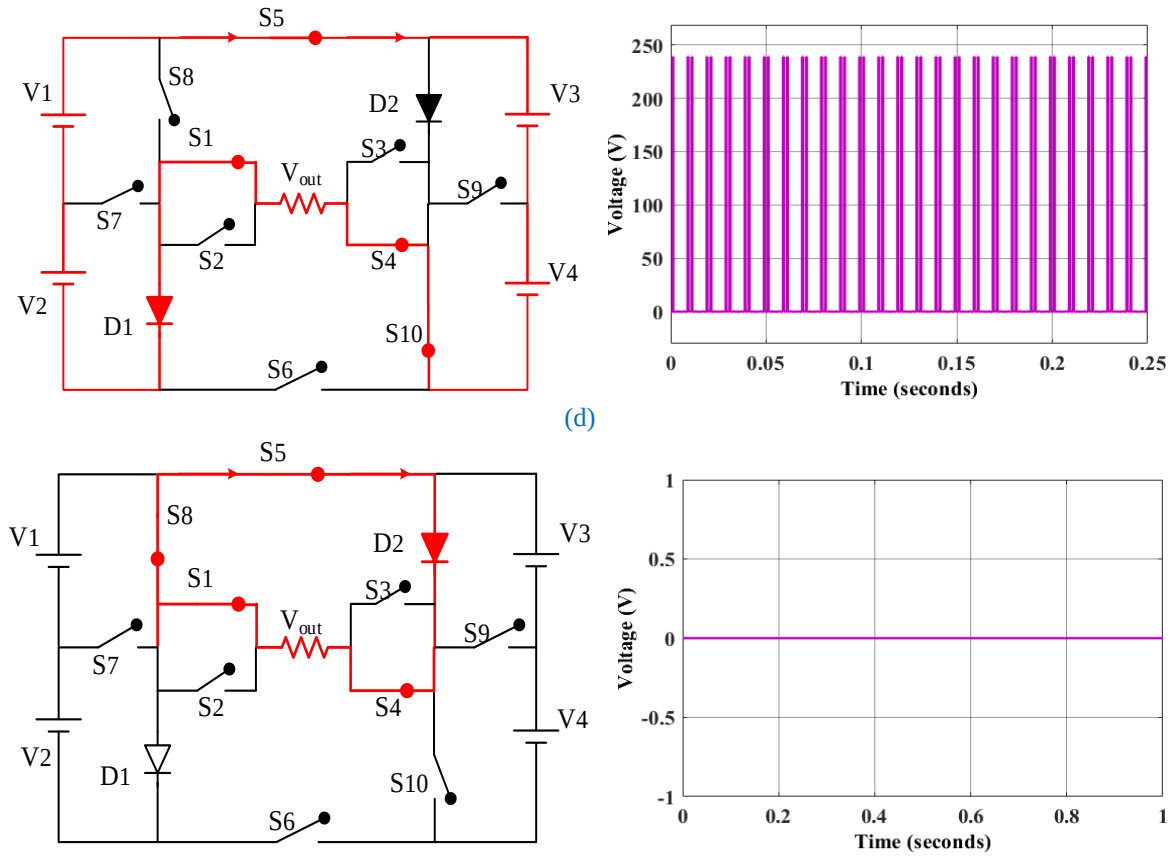

Figure 4: Modes of operation of proposed inverter (a) mode 1 (b) mode 2 (c) mode 3 (d) mode 4 (e) mode 5

A low voltage of zero and a high voltage of 240 V are both produced by the suggested topology. The 51-level inverter's several modes of operation are illustrated in Figure 4. Mode 1 uses a single voltage source to produce a 30V output. In the first mode, all but switches S1, S4, S5, and S7 are disabled. In mode 2, a 60V output voltage was produced by conducting two voltage sources. During mode 2, only switches S1, S4, and S5 are operational; all others are disabled. Using V1, V2, and V3 as inputs, Mode 3 generated an output voltage of 150 V. Switches like S1, S9, S5, and S4 are under on condition, and others are under off condition in Mode 3. All voltage sources operate in Mode 4 and produce a maximum output voltage of 240V. Switches S4, S5, S1, and S10 are all turned on in this mode.Mode 5 represents the zero state, which generates zero voltage as an output because no voltage sources are conducted. Only switches S1, S4, S5, and S8 are active in this first mode; all others are inactive. As more voltage levels are added and the voltage waveform gets closer to a sine wave, the output voltage becomes better.

Power losses of any semiconductor switch, IGBT, can be divided into conduction losses and switching losses [26]. Instead, these are combined as the total power loss of the MLI (T_{Loss}) , as expressed in equation (18).

$$T_{LOSS} = T_{Conduction} + T_{Switching} \quad (18)$$

where, $T_{Switching}$ denotes switching loss and $T_{Conduction}$ represent conduction loss in the proposed inverter. The efficiency of the MLI is calculated using the following equation (19).

$$Efficiency = \frac{P_{Output}}{P_{Output} + T_{LOSS}} \times 100 \quad (19)$$

DOI: 10.46121/pspc.53.4.22

where, P_{Output} indicates output power. The loss and efficiency of the proposed MLI are evaluated using the above equations [31]. The proposed inverter achieves an efficiency of 95.653%. This efficiency is based on a total conduction loss of 71.98 W and a total switching loss of 0.73 W, resulting in total power losses of 72.71 W.

3.5 Proposed Control Strategy

A master unit's primary responsibility in microgrid isolated mode is to maintain a constant frequency and voltage at the Point of Common Coupling (PCC).As an inverter for voltage sources, the main unit can only be used in voltage control mode [30]. It is recommended that the master unit operate in current control mode (as a current source inverter) while the microgrid is connected to the grid.Since the slave units are responsible for injecting power, the steady-state current of the master unit should be zero when in islanded mode. Slave inverters in a master-slave architecture control the amount of current that can reach the loads. Consequently, the designated individuals bear the responsibility of introducing both reactive and active electrical energy into the interconnected loads through the PCC. In order to maintain a stable, balanced, and reliable voltage at the PCC, the master unit supplies the reference voltage to the slave units. Furthermore, the slave units function alone in both grid-connected and islanded modes under the present control mode. In this work, a cascaded TFOPI-FOTD controller is proposed to control the switching pulses of novel MLI. Gain parameters of this controller like K_{t1}, K_p, K_i, K_{t2}, K_d, N, λ and μ are tuned using the FHO algorithm.

3.5.1Cascaded TFOPI-FOTD controller

Fractional calculus can be defined through several approaches, with the most prominent ones being the Riemann–Liouville definitions. The proposed cascaded TFOPI-FOTD controller is designed to regulate the output voltage of the MLI. The controller consists of two cascaded stages: a TFOPI stage and a FOTD stage. Equation (20) defines this operator in such a way that fractional derivatives and fractional integrals can be applied simultaneously.

$$ {}_aD_b^{\alpha}\ f(t) = \frac{1}{\Gamma(m-\alpha)}\frac{d^m}{dt^m}\int_a^b \frac{f(\upsilon)}{(t-\upsilon)^{\alpha+1-m}}d\upsilon, \quad (20)$$

where, m denotes the integer part of α, $m-1<\alpha<m, m\in N$, $f(t)$ denotes the function, and $\Gamma(x)$ indicates the Euler's gamma function of x. Equation (21) presents the generalized transfer function of the TFOPI.

$$C^{TFOPI}(s) = \frac{K_{t1}}{\frac{1}{s^N}} + \left(K_p + \frac{K_i}{s^{\lambda}}\right) \quad (21)$$

The FOTD controller's transfer function is as follows.

$$C^{FOTD}(s) = \frac{K_{t2}}{\frac{i}{s^N}} + K_d s^{\mu} \quad (22)$$

The transfer function of the proposed cascaded T-FOPI-FOTD controller is given by

$$C^{TFOPI-FOTD}(s) = \frac{K_{t1}}{\frac{1}{s^N}} + \left(K_p + \frac{K_i}{s^{\lambda}}\right) + \frac{K_{t2}}{\frac{i}{s^N}} + K_d s^{\mu} \quad (23)$$

where, K_{t1} indicates tilt gain for TFOPI controller, K_p denotes proportional gain, K_i represent integral gain, K_{t2} represent tilt gain for FOTD controller, and K_d means derivative gain parameter [27]. The adjustable parameter N is preferably chosen between 2 and 3. Moreover, it includes two additional coefficients, λ and μ which are defined in the computation of the differ-integral order function. According to fundamental principles, the proposed controller maintains system stability. Figure 5 represents the structure of the proposed cascaded controller.

DOI: 10.46121/pspc.53.4.22

Power System Protection and Control
ISSN:1674-3415

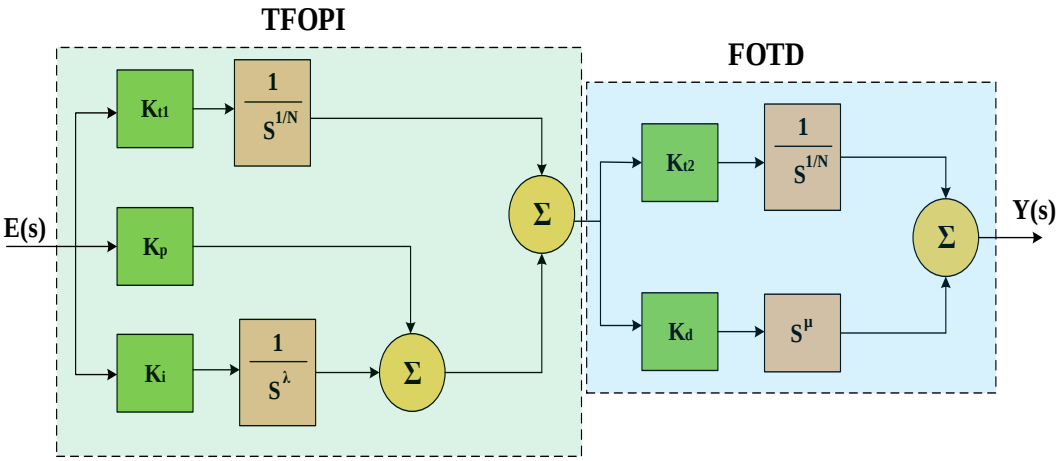

Figure 5. Structure of proposed cascaded controller

C-TFOPI-FOTD controller governs the AC bus voltage by regulating the output of each inverter. The controller continuously monitors the AC bus parameters and adjusts the reference signals applied to the three inverters. For synchronization, a PLL mechanism generates a common reference angle, and each inverter adjusts its modulation index and phase accordingly. Inverter near PV source is regulated via the DC–DC converter and RNN-based MPPT to supply stable DC power, with its inverter output phase-aligned to the bus. Inverter in wind source through rectifier is synchronized using the PLL reference, ensuring frequency and phase alignment. Inverter in battery through bidirectional DC–DC converter operates as a balancing unit, injecting or absorbing power based on bus demand, while also tracking the common AC bus angle. This coordinated control strategy ensures stable AC bus voltage, smooth synchronization among the three sources, and effective power sharing under dynamic operating conditions. However, to enhance the controller's efficiency, the gain parameters of the proposed controller are selected using an optimization algorithm. Therefore, this work utilized the FHO algorithm.

3.5.2 Fire Hawks Optimization (FHO)

The FHO is a widely used metaheuristic optimization algorithm suitable for tuning the gain parameter of a C-TFOPI-FOTD controller, achieving minimal error and reduced harmonics [28]. To achieve precise error minimization, the proposed approach aims to optimize the constraints on proportional, integral, tilt, and derivative gains $\left(\mathrm{K}_p, \mathrm{K}_i, \mathrm{K}_t, \mathrm{K}_d\right)$ of the C-TFOPI-FOTD controller.The 51-level inverter was chosen for its ability to produce a higher quality output voltage with lower THD compared to lower-level inverters. The FHO algorithm was selected for its fast convergence rate, global optimization capability, and robustness to local minima, which are critical for controller gain tuning. Unlike GA or PSO, which may stagnate in local minima, FHO dynamically adapts its search strategy, making it more reliable for the nonlinear optimization problem of switching state selection.It imitates the way that solitary hawks forage, which includes starting and maintaining flames in order to capture prey. The initial vector starting positions within the search space are identified by an initial randomization technique. It is computed and expressed as;

$$\mathrm{Y} = \begin{bmatrix} \mathrm{Y}_1 \\ \mathrm{Y}_2 \\ \vdots \\ \mathrm{Y}_j \\ \vdots \\ \mathrm{Y}_\mathrm{N} \end{bmatrix} = \begin{bmatrix} y_1^1 & y_1^2 & \cdots & y_1^k & \cdots & y_1^e \\ y_2^1 & y_2^2 & \cdots & y_2^k & \cdots & y_2^e \\ & & \vdots\vdots\vdots & \ddots & \vdots & \\ y_j^1 & y_j^2 & \cdots & y_j^k & \cdots & y_j^e \\ & & \vdots\vdots\vdots & \ddots & \vdots & \\ y_\mathrm{N}^1 & y_\mathrm{N}^2 & \cdots & y_\mathrm{N}^k & \cdots & y_\mathrm{N}^e \end{bmatrix} \tag{24}$$

$$y_j^k(0) = y_{j,MIN}^k + R.\left(y_{j,MAX}^k - y_{j,MIN}^k\right), \begin{cases} j = 1,2,\ldots\ldots, \mathrm{N} \\ k = 1,2,\ldots\ldots\ldots, e \end{cases} \tag{25}$$

DOI: 10.46121/pspc.53.4.22

Power System Protection and Control
ISSN:1674-3415

From the above equation, jth candidate solution within the search space is represented by Y_j, the dimensionality of the problem is denoted by ℓ, and the number of the candidate solutions is denoted by N. The initial positions of the candidate solution are denoted by $y_j^k(0)$, y_j^k represents the kth decision variable of jth candidate solution as well as R indicates the random number lies between the range of 0 to 1. The maximum and minimum bounds within the jth candidate solution for kth decision variable is $y_{j,MAX}^k$ and $y_{j,MIN}^k$. To help hunters find their prey, Fire Hawks are used to spread fires across the area where they are looking. The main fire that Fire Hawks use to cover the search area with flames is also thought to be the best gain measure [29]. Then, it is expressed as;

$$\mathrm{P}R = \begin{bmatrix} \mathrm{P}R_1 \\ \mathrm{P}R_2 \\ \vdots \\ \mathrm{P}R_l \\ \vdots \\ \mathrm{P}R_n \end{bmatrix}, \qquad l = 1,2,\ldots..,n \quad (26)$$

$$F\mathrm{H} = \begin{bmatrix} F\mathrm{H}_1 \\ F\mathrm{H}_2 \\ \vdots \\ F\mathrm{H}_m \\ \vdots \\ F\mathrm{H}_o \end{bmatrix}, \qquad m = 1,2,\ldots...., o \quad (27)$$

where, $F\mathrm{H}_1$ denotes the mth fire hawk in the search space for fire hawks n, $\mathrm{P}R_l$ indicates the lth prey with the search space based on the wholeamount of n preys. The total distance among fire hawks and prey is calculated and expressed as below:

$$d_l^1 = \sqrt{(y_2 - y_1)^2 + (z_2 - z_1)^2}, \quad \begin{cases} m = 1,2,\ldots., m \\ l = 1,2,\ldots., n \end{cases} \quad (28)$$

From the above equation, the wholeamount of fire hawks and prey is denoted by 0 and η. The distance among l^{th} prey and m^{th} fire hawk is represented by d_l^1, and the coordinates of fire hawks and prey are indicated by (y_2, z_2) and (y_1, z_1).

$$F\mathrm{H}_m^{NEW} = F\mathrm{H}_m + (\gamma_1 \times G_b - \gamma_2 \times F\mathrm{H}_{near}) \quad m = 1,2,\ldots.o \quad (29)$$

The best gain parameter is represented by G_b, the position vector for m^{th} fire hawk ($F\mathrm{H}_m$) is represented by $F\mathrm{H}_m^{NEW}$, the random numbers are uniformly distributed, and it is indicated as γ_1 and γ_2.

$$\mathrm{P}R_r^{NEW} = \mathrm{P}R_r + (\gamma_3 \times F\mathrm{H}_1 - \gamma_4 \times sp_m) \quad \begin{cases} m = 1,2,\ldots., o \\ r = 1,2,\ldots...., \gamma \end{cases} \quad (30)$$

From the above equation, the best gain parameter is denoted as G_b, updated position for the γ^{th} prey ($\mathrm{P}R_r$) is represented by $\mathrm{P}R_r^{NEW}$, the random integers lying among the range 0 to 1 is denoted by γ_3 and γ_4, sp_m indicates the secure location within the region of the m^{th} Fire Hawk.

DOI: 10.46121/pspc.53.4.22

$$PR_r^{NEW} = PR_r + \left(\gamma_5 \times FH_{ALTER} - \gamma_6 \times sp\right) \quad \begin{cases} m = 1,2,....,o \\ r = 1,2,....., \gamma \end{cases} \quad (31)$$

The random integers lie among the range 0 to 1 and are denoted by γ_5 and γ_6. FH_{ALTER} indicates one of the fire hawks in the search area; sp denotes a secure location beyond the terrain of the m^{th} Fire hawks.

The mathematical representation of sp_m and sp is derived from the principle that animals commonly group in a safe location to protect themselves from danger, and it is expressed as;

$$sp_m = \frac{\sum_{r=1}^{\gamma} PR_r}{\gamma}, \quad \begin{cases} r = 1,2,....., \gamma \\ m = 1,2,....., o \end{cases} \quad (32)$$

$$sp = \frac{\sum_{l=1}^{n} PR_l}{n}, \quad l = 1,2,...., n \quad (33)$$

From the above equation, PR_r represent the γ^{th} prey surrounded by m^{th} Fire Hawk and the l^{th} prey within the search space is mentioned by PR_l.

RESULTS AND VALIDATION

The suggested project makes use of the MATLAB/Simulink software. The suggested inverter and controller proved the feasibility of the hybrid system, which combined wind and solar power in an isolated community microgrid. The parameters used to build the proposed controller are displayed in Table 3. The proposed work's Simulink block diagram is displayed in Figure 6.

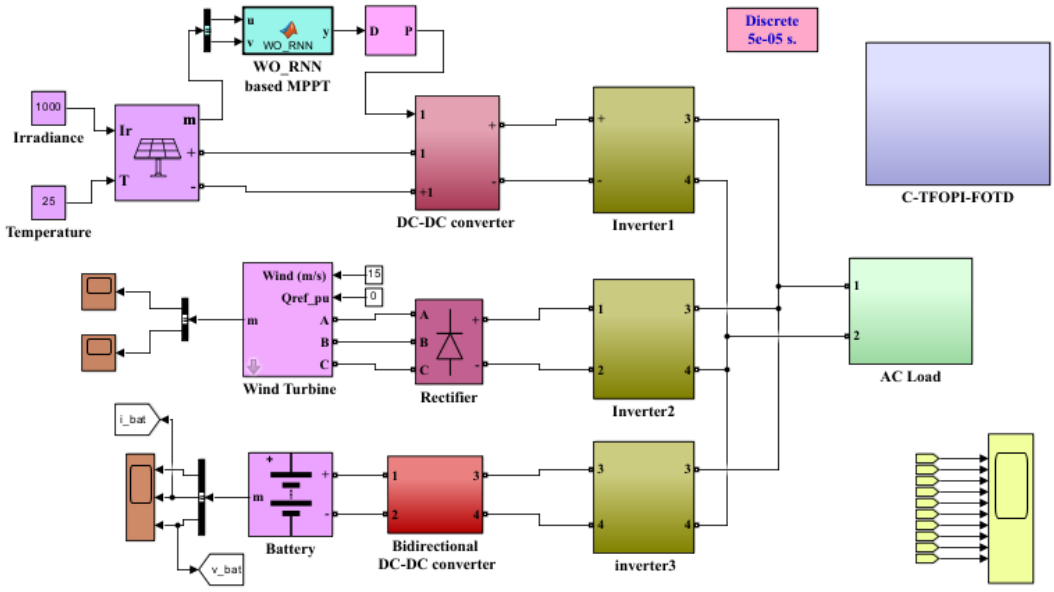

Figure 6: Simulink block diagram for proposed work

Table 3. System parameter

Description	Parameters	Value
PV	Maximum power	213.15 W
	Open circuit voltage	36.3 V
	Short-circuit voltage	7.84 A
	Voltage at MPPT	29 V

DOI: 10.46121/pspc.53.4.22

Power System Protection and Control
ISSN:1674-3415

Battery	Nominal voltage	200V
	Rated capacity	14 Ah
Wind	stator	0.023 p.u
	inductance	2.9 p.u
	Wind speed	15m/s

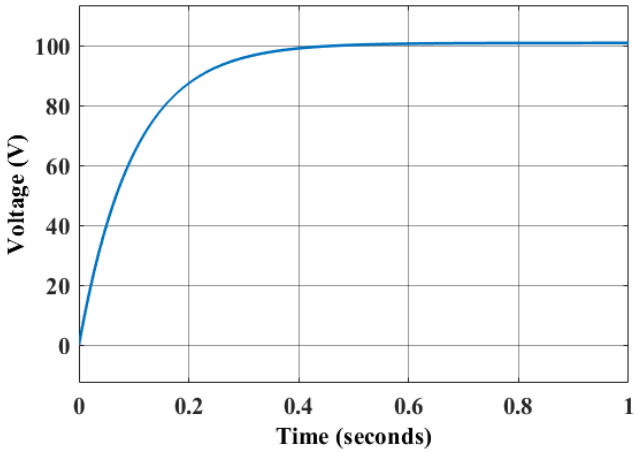

Figure 7. PV voltage

Figure 7 illustrates the analysis of PV voltage. This graph shows a solar PV panel working at a continuous irradiation level of 1000 W/m^2. The voltage begins at 0 volts and gradually increases to 100 V. The PV voltage is obtained to enhance the MPPT performance, optimize system design, and facilitate battery charging. The graph shows the voltage of a system of a system reaching a steady state, the finalvalue of the voltage after the transient response is 100V.

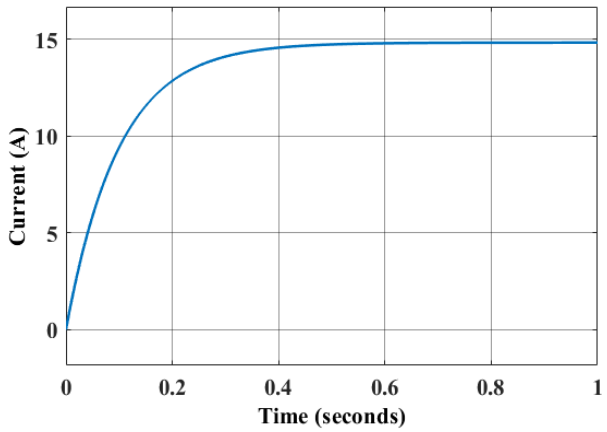

Figure 8. PV current

Figure 8 provides the analysis of PV current. This graph illustrates the solar PV panel operating under a consistent irradiation level of 1000 W/m². In this graph, the current is increased from 0 to 14 A. An increasing PV current is utilized to enhance power output and improve system flexibility and efficiency. This shows that the current has reached a stable or steady state conditions. The graph clearly shows the current of the system stabilizing overtime.

DOI: 10.46121/pspc.53.4.22

Power System Protection and Control
ISSN:1674-3415

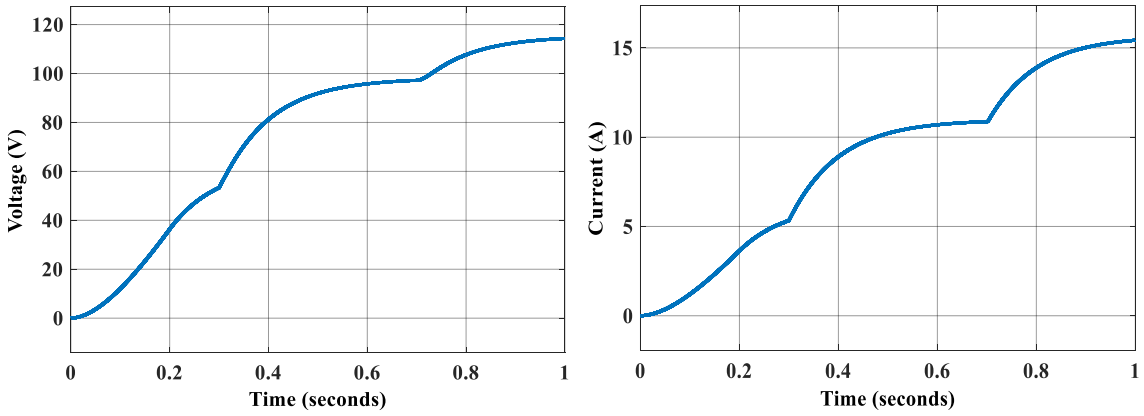

(a) (b)

Figure 9:Varying irradiance for solar PV (a) Voltage (b) current

Figure 9 shows the varying irradiance for solar PV (a) Voltage (b) current. Subplot (a) shows the voltage characteristics of solar panel under varying irradiance. The voltage ranges from 0 to 120 V and the times varies from 0 to 1 sec. At 0.3 sec, the voltage 50V when the irradiance reaches 400W/m^2. Then the irradiance is varied to 700W/m^{2}the voltage is approximatly 95V at 0.7 sec. Then the irradiance is varied 700W/m^2. Subplot (a) shows the voltage characteristics of solar panel under varying irradiance. The current ranges from 0 to 15A and the times varies from 0 to 1 sec. At 0.3 sec, the current 5A when the irradiance reaches 400W/m^2. Then the irradiance is varied to 700W/m^2 the voltage is approximatly 11A at 0.7 sec. Then the irradiance is varied 700W/m^2.

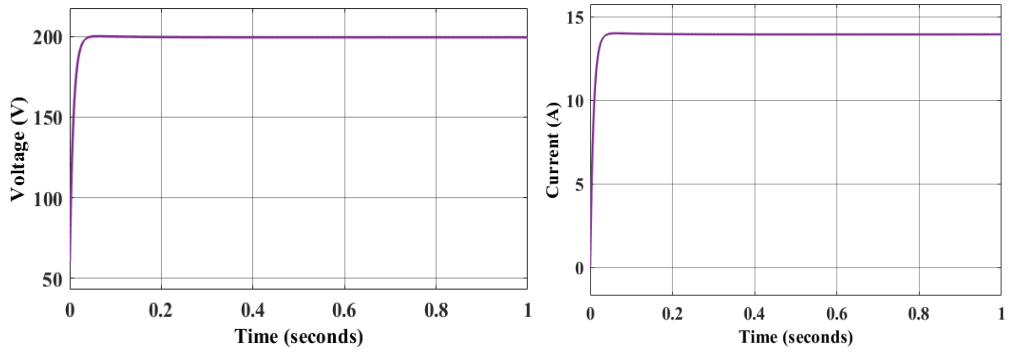

(a) (b)

Figure 10: Output of DC to DC converter

The DC-to-DC converter's voltage and current output at a constant irradiance level are shown in Figure 10. This converter obtained a high range of output power by the use of walrus optimized RNN based MPPT method. This method optimally selected the best duty cycle to generate a high range of output. Results analysis shows that the converter provides the output current and voltage of 14A and 200V. Thus, a high range of output power is obtained from solar panels.

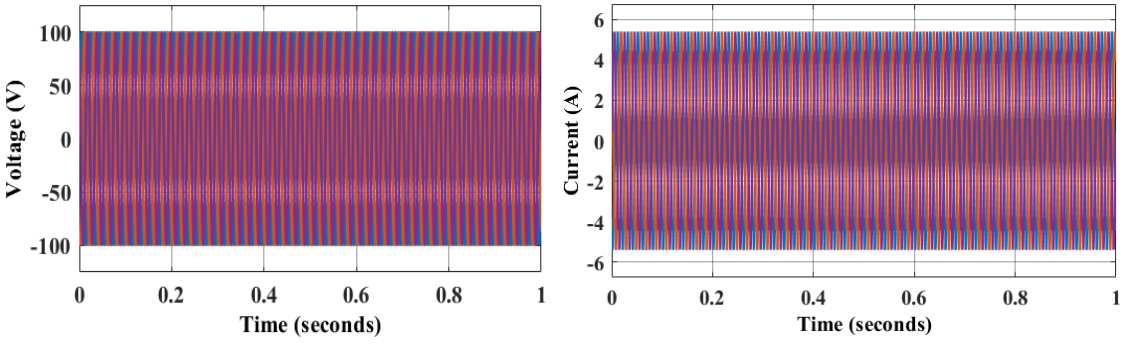

(a) (b)

Figure 11: Characteristic response of wind turbine (a) voltage (b) current

DOI: 10.46121/pspc.53.4.22

Power System Protection and Control
ISSN:1674-3415

Figure 11 shows the wind turbine's input and output at a continual wind speed. Graph (a) indicates the voltage waveform oscillating between +100 V and -100 V, which has a peak amplitude of 100 V, while graph (b) indicates the current waveform oscillating between +5A and -5A, which has a peak amplitude of 5 A. The wind speed is set at 15m/s, and the wind turbine generates 540W of power at this speed.Wind turbines provide 100V of output voltage and 5.4A of current, respectively. These measurements indicate the peak magnitudes of the voltage and current signals, respectively, in their continuous oscillations.

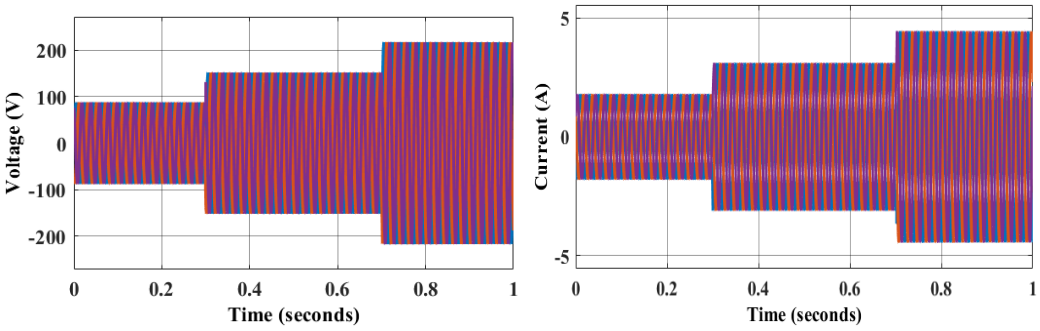

(a) (b)

Figure 12:Varying wind speed in wind turbine (a) Voltage (b) Current

Figure 12 shows the varying wind speed in wind turbine (a) voltage (b) current. Subplot (a) shows the voltage by varying the wind speed.The voltage waveform oscillating between -200 V and +200 V,Upto 0.3 sec the wind speed is 10m/s. Upto 0.7sec it has the wind speed of 12m/s then it has 15m/s.Subplot (b) shows the current by varying the wind speed.The current waveform oscillating between -5A and +5A.

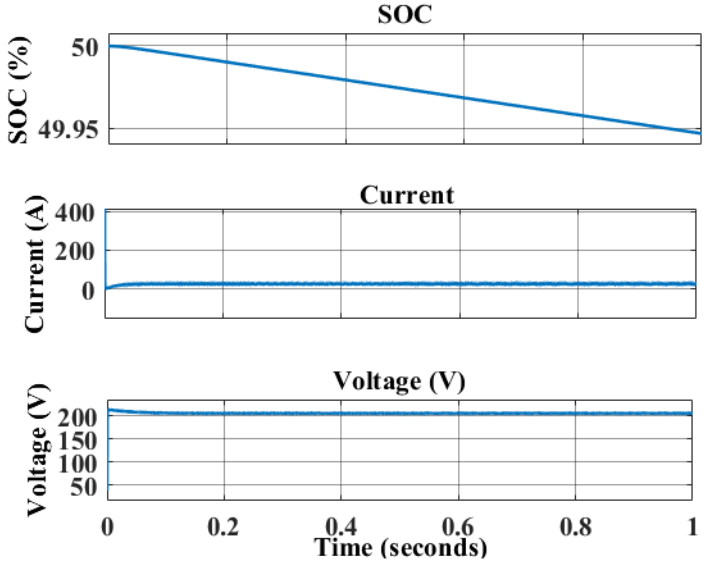

Figure 13: Characteristic output of battery

Figure 13 represents the output of the battery in the master unit. This figure shows the battery's output voltage, current, and state of charge. The bidirectional converter is used to maintain the energy balance of the islanded microgrid. In this work, the battery acts as a master and hybrid renewable energy sources are considered slave units. Excess power PV and wind sources are stored in the battery. During high demand times, the battery satisfies the load demand if hybrid source power is not enough.

DOI: 10.46121/pspc.53.4.22

Power System Protection and Control
ISSN:1674-3415

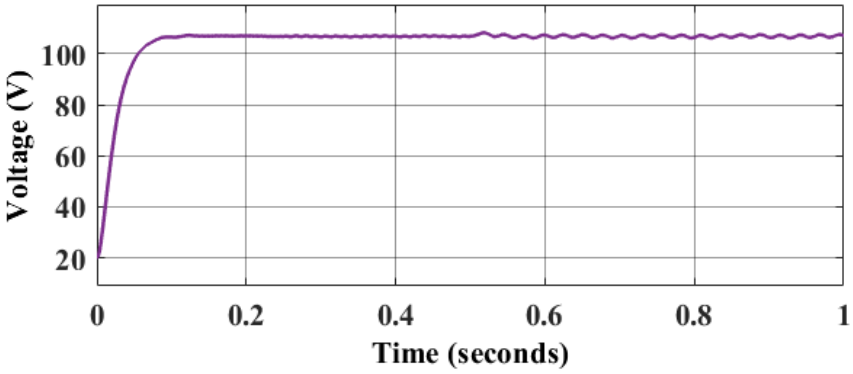

Figure 14:Reverse DC-to-DC converter output

The output voltage of the bidirectional DC to DC converter is given in Figure 14.The plot demonstrates a system's voltage response within 1 second, with the voltage starting near 0 V, rising rapidly, and finally stabilizing at a steady value of 110 V. The x-axis represents time in seconds, and the y-axis represents voltage in volts. As time progresses, the voltage curve approaches the 110 V position, in small rapid oscillations, or ripple, close to this value. These little oscillations have no effect on the general steady-state, and the graph shows that the system reaches a stable final voltage of 110 V once the initial transient response is over.

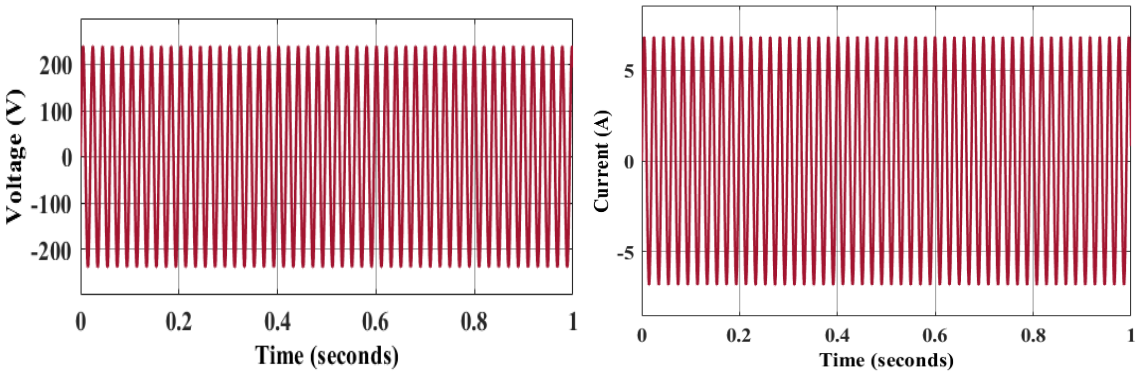

(a) (b)

Figure 15: Proposed 51-level inverter output (a) voltage (b) current

Figure 15 shows the output characteristics of the suggested 51-level asymmetric inverters. Figure 15(a) shows the proposed 51-level inverter's output voltage waveform over a period of 1sec. The voltage is stepped sinusoidal, as is the case in multilevel inverters. The peak-to-peak voltage is approximately 400 V and varies from around +200 V to -200 V. The accompanying current waveform over the same 1-second interval is shown in Figure 15(b). As with the voltage, the current is also a stepped sinusoid of approximately 10A peak-to-peak value, oscillating between +5A and -5A. The proposed FHO optimized cascaded controller generates this optimal 51 level step output with less THD. The characteristic response was obtained for a period of 1 seconds.

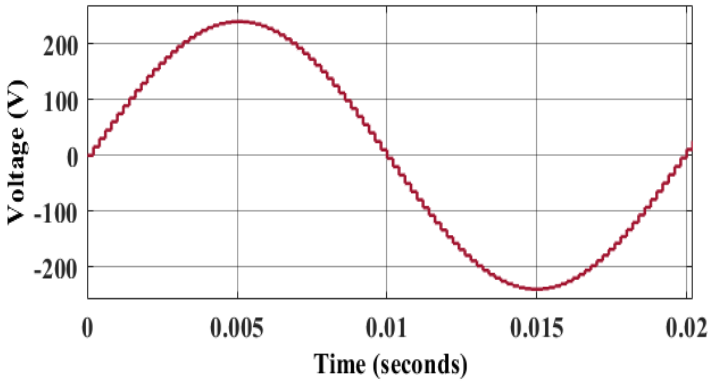

Figure 16: Output voltage of inverter

DOI: 10.46121/pspc.53.4.22

Power System Protection and Control
ISSN:1674-3415

The zoomed-in output voltage of the proposed inverter is illustrated in Figure 16. The stepped profile of the voltage is evident, with discrete levels closely approximating a sinusoidal waveform. The output voltage peaks at around +220V and drops to around -220V and the X-axis ranges from 0 to 0.02 sec.The availability of 51 voltage levels makes the output waveform closely mimic the form of a pure sine wave. With more levels, harmonic distortion is reduced, resulting in better power quality.

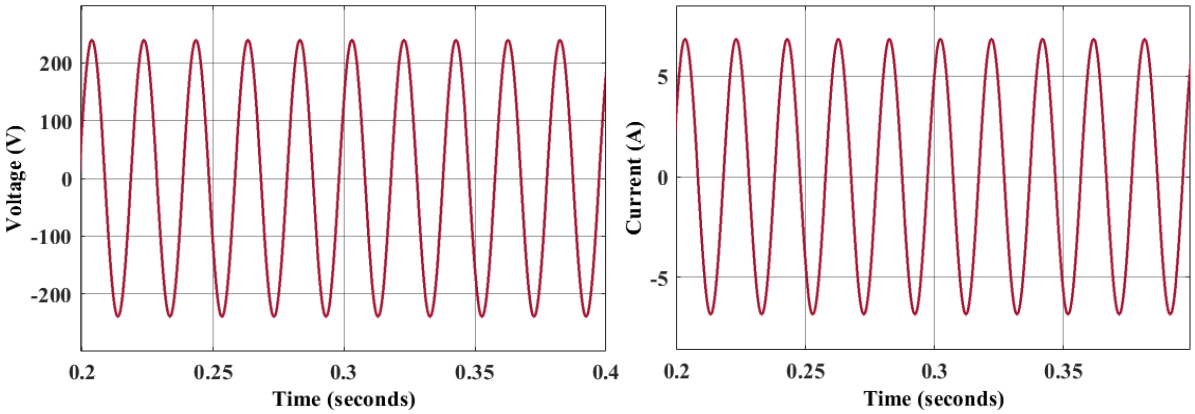

Figure 17: Simulation results of the MLI's output voltage and current under resistive load conditions.

Figure 17 represents the simulation output of MLI output voltage and current under the resistive (R=200Ω) load condition. The simulation outcomes confirm that the proposed 51 MLI provides sinusoidal output voltage and current in resistive load conditions. The inverter produces a peak output voltage of approximately 220V and a peak current of nearly 5A, with synchronized and in-phase waveforms for voltage and current, thus verifying resistive load operation.

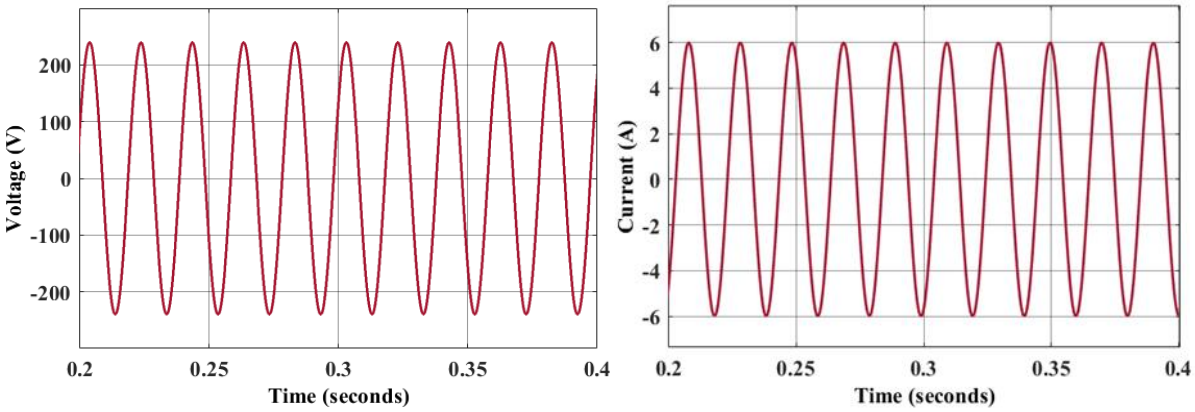

Figure 18: MLI's output voltage and current under RL load

Figure 18 illustratesMLI's output voltage and current under the resistive inductive (R=200Ω, L=200mH) load condition. These figures illustrate the in-phase relationship between voltage and current, confirming the expected behavior under R and RL load. The figures demonstrate the phase shift and smoothing effect on the output current, showcasing the MLI's performance under a more complex load.

DOI: 10.46121/pspc.53.4.22

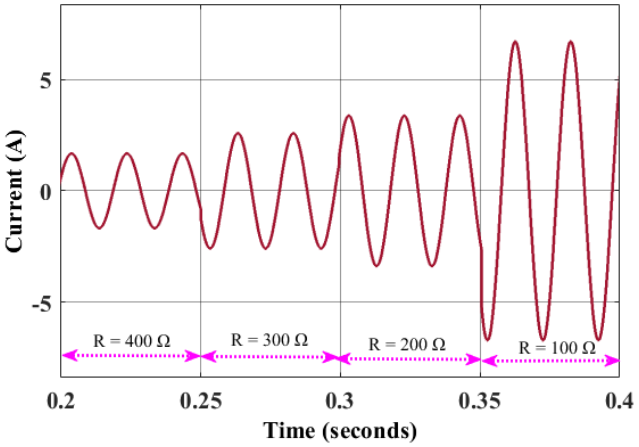

Figure 19:Simulated current waveform under dynamic R-load conditions

Figure 19 depicts the dynamic response of current within an electrical circuit subjected to stepwise reductions in resistance. This figure illustrates the current waveform over a time interval of 0.2 to 0.4 seconds, during which the circuit's resistance is progressively decreased from 400 Ω to 100 Ω in 100 Ω increments. Initially, with a resistance of 400 Ω, the current exhibits a relatively low amplitude sinusoidal waveform. As the resistance is reduced to 300 Ω, 200 Ω, and finally 100 Ω at approximately 0.25, 0.3, and 0.35 seconds, respectively, a corresponding increase in the current's amplitude is observed.

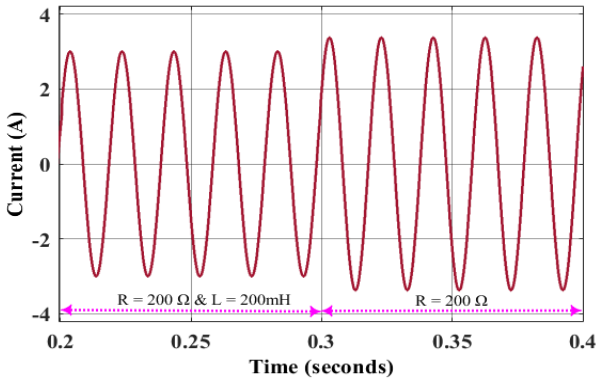

(a)

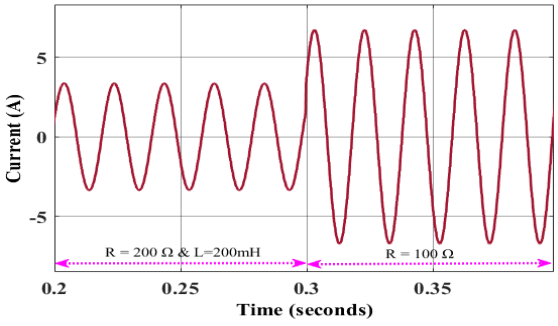

(b)

Figure 20: Simulated output current during dynamic load change (a) RL to R, R=200Ω (b) RL to R, R=100Ω

Figure 20 illustrates the current response to a change in load parameters within an electrical circuit. The sinusoidal waveform signifies an AC behavior, driven by an AC voltage source. Two distinct regions are observed, representing an RL load (with a resistor and inductor) and an R load (with only the resistor). At approximately 0.3 seconds, the inductor is removed, leading to notable changes in the current waveform. The removal likely reduces or eliminates the phase shift between currents, as in a purely resistive circuit, they are in phase. This analysis effectively demonstrates the transient response of the current to load parameter changes, highlighting the

DOI: 10.46121/pspc.53.4.22

impact of the inductor on the circuit's behavior. Using the proposed control strategy, these load variations are effectively handled.

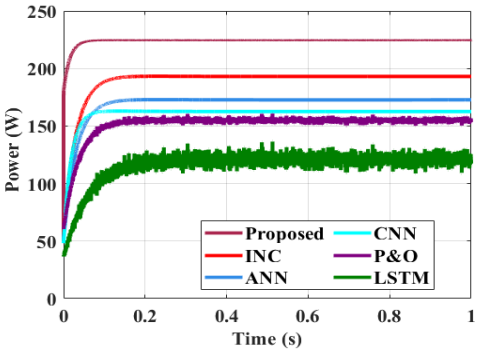

Figure 21: Comparative analysis of MPPT

The comparative study of MPPT is shown in Figure 21. The proposed method is compared with various approacheslike INC, P&O, Convolutional neural network (CNN), long short term memory (LSTM) and Artificial Neural Networks (ANN). In contrast, the proposed technique demonstrates superior tracking capability, potentially enhancing overall system efficiency compared to existing methods.The findings prove that the proposed model performs better than all the other methods compared by always has the highest and most consistent power from the PV system. It largely outperforms conventional methods like P&O,INC, ANN, CNN, and LSTM.

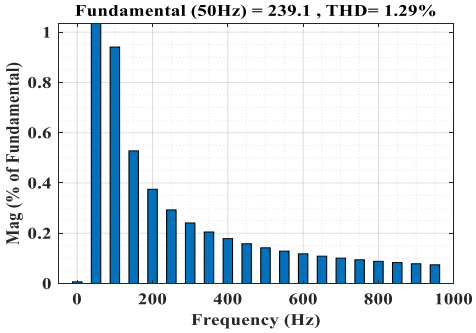

Figure 22: THD analysis for voltage

The THD analysis of the voltage for 51 level MLI is shown in Figure 22. From this graph, the results showed that the fundamental voltage obtained is 239.1 V and a THD of 1.29% for that fundamental voltage. It indicates that the inverter produces a high-quality voltage waveform with minimal harmonic distortion, ensuring reliable operation and maximizing energy conversion stability from the renewable energy source.

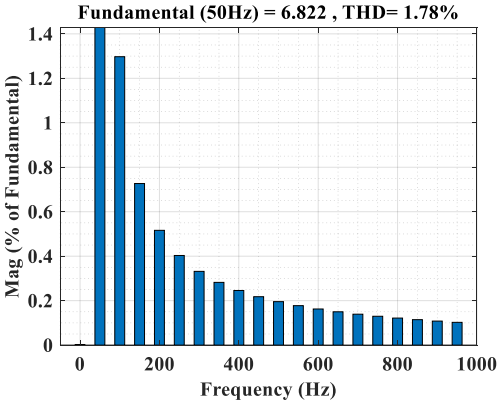

Figure 23: THD analysis for the current

Figure 23 presents the THD analysis of the current for a 51-level MLI. The analysis indicates a fundamental current of 6.822 A with a THD of 1.78% relative to this fundamental current. These results showed that the inverter

DOI: 10.46121/pspc.53.4.22

Power System Protection and Control
ISSN:1674-3415

can maintain a primary current component while minimizing harmonic distortion, which is essential for stable performance.

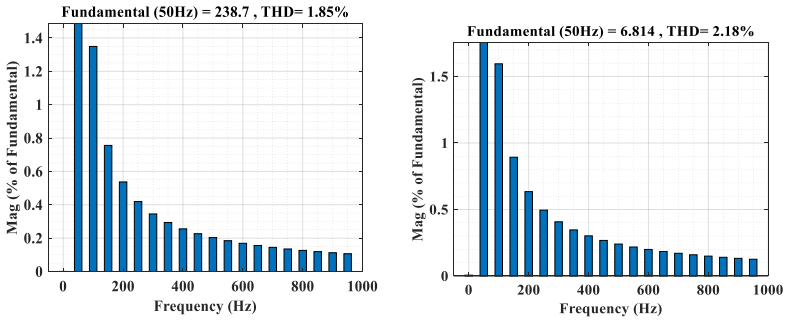

(a) (b)

Figure 24: THD analysis for TFOPI (a) voltage (b) current

Figure 24 provides the THD analysis for TFOPI. In Figure 24(a), the findings indicated that the fundamental voltage obtained is 238.7 V and a THD of 1.85% for that fundamental voltage. In Figure 24(b), the results show that the fundamental current is 6.814 A, with a THD of 2.18% for that current. When compared to the proposed technique, the existing technique has higher THD.

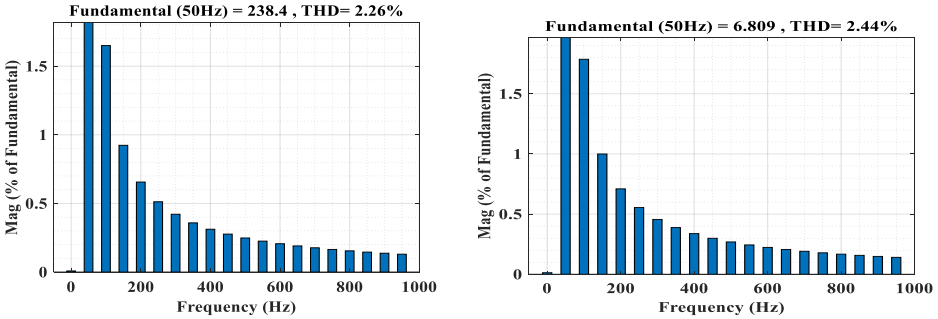

(a) (b)

Figure 25: THD analysis for FOTD (a) voltage (b) current

Figure 25displays the THD analysis for FOTD. In Figure 25(a), the analysis reveals a fundamental voltage of 238.4 V with a THD of 2.26%. In Figure 25(b), the fundamental current is measured at 6.809 A with a THD of 2.44%. These results indicate that compared to the proposed technique, the existing method exhibits higher THD levels. This suggests that the proposed technique may offer better performance in maintaining lower harmonic distortions in both voltage and current, which is critical for enhancing the reliability and efficiency of power systems.

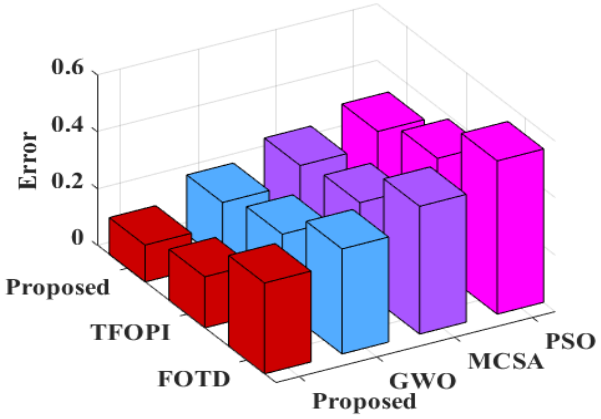

Figure 26: Comparative analysis of error performance

DOI: 10.46121/pspc.53.4.22

Power System Protection and Control
ISSN:1674-3415

Figure 26 provides a comparative analysis of error performance among different control and optimization techniques. The error, which quantifies the deviation from the desired performance objective, serves as the metric for comparison. Lower error values indicate better performance, reflecting a closer match to the target or a more accurate control action. The 3D bar chart visually represents the error for each technique, with the height of each bar corresponding to the magnitude of the error. The results show that the proposed method exhibits the lowest error, indicating its superior accuracy and effectiveness in achieving the desired control outcome. In contrast, other techniques, including TFOPI, FOTD, GWO, MCSA, and PSO, show significantly higher error values, suggesting their relative inferiority in achieving precise control.

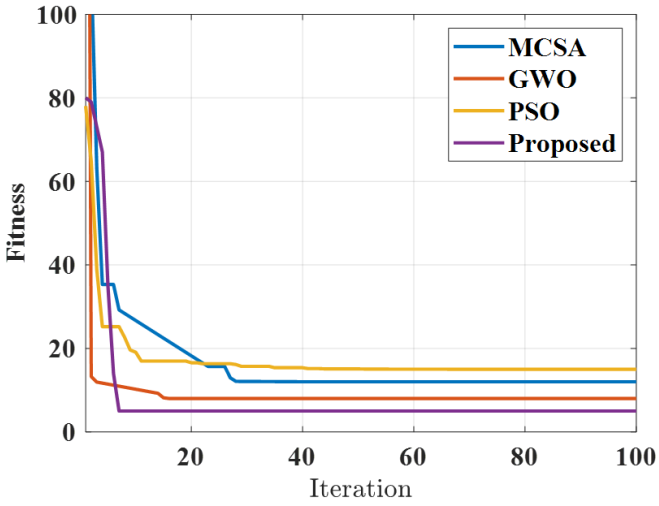

Figure 27: Convergence of FHO

Figure 27 depicts the convergence plot of FHO, where MCSA is the multi-strategy boosted chameleon-inspired optimization algorithm, PSO, and GWO. Using FHO, the minimum fitness is achieved by the 8th iteration. Existing optimizations like MCSA, PSO, and GWO require more iterations of 28, 41, and 15, respectively. Figure 26 represents the Comparative analysis of THD voltage and current with different controllers. By minimizing THD in both current and voltage, the suggested method attains a maximum voltage of 239.1 V. This indicates that the proposed technique is highly effective in maintaining power quality and stability. The TFOPI technique shows slightly lower voltage and higher THD for both voltage and current compared to the proposed technique. This means that although it performs relatively well, it is not as efficient or effective in minimizing harmonic distortions as the proposed technique. The FOTD technique has the lowest voltage among the three techniques and the highest THD for both voltage and current. This suggests that it is the least efficient in maintaining power quality and minimizing distortions.

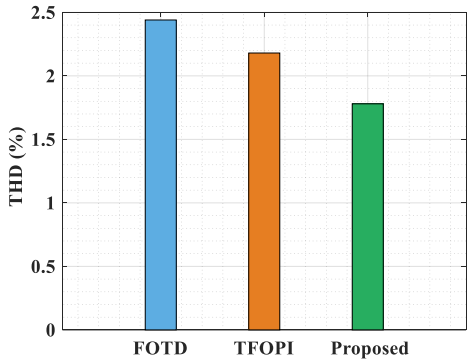

(a)

DOI: 10.46121/pspc.53.4.22

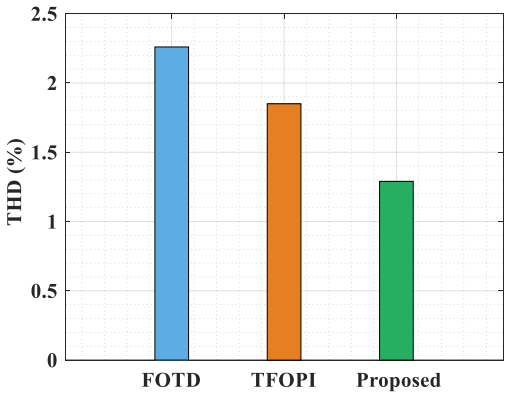

(b)

Figure 28: Comparative analysis of THD (a) voltage (b) current

Table 4. Comparative analysis

Technique	Voltage (V)	THD for voltage	Current (A)	THD for current
Proposed	239.1	1.29%	6.822	1.78%
TFOPI	238.7	1.85%	6.814	2.18 %
FOTD	238.4	2.26%	6.809	2.44%

Table 4 shows a comparison of several methods according to voltage, THD of voltage, and current. The evaluation focuses on output voltage, voltage THD, output current, and current THD. Notably, the proposed technique demonstrates superior performance across all metrics. It achieves an output voltage of 239.1 V, the highest among the three, coupled with the lowest voltage THD of 1.29%. Simultaneously, it delivers an output current of 6.822 A with a current THD of only 1.78%, again the lowest observed.

In contrast, TFOPI exhibits a slightly lower output voltage of 238.7 V, accompanied by higher THD values: 1.85% for voltage and 2.18% for current. FOTD shows the least favorable performance, with an output voltage of 238.4 V and the highest THD values, 2.26% for voltage and 2.44% for current. These results clearly indicate that the proposed technique effectively minimizes harmonic distortion, resulting in improved power quality compared to the TFOPI and FOTD methods.

CONCLUSION

This work proposed a 51-level asymmetrical MLI topology combines with the WO-RNN based MPPT and fire hawks optimization based C- TFOPI-FOTD controller which demonstrates the significant improvement in efficiency and reduces the power losses. The simulation output confirms the system's strength under different conditions, and it achieves a high voltage output of 239.1 V with an extremely low THD of 1.29% for voltage and 1.78% for current. These values reflect better waveform quality, less harmonic content, and better stability compared to traditional control methods. In addition, the novel approach performs better than TFOPI and FOTD controllers that achieved higher voltage THDs of 1.85% and 2.26%, and current THDs of 2.18% and 2.44%, respectively. The system also obtains a total efficiency of 95.653% due to the fewer number of switches and conduction losses in the presented MLI structure. These results confirm that the presence of state-of-the-art optimization and smart control algorithms in the inverter design assures high reliability, low distortion, and efficient energy conversion, which makes the suggested system a promising candidate for renewable energy-based microgrids.In the future, it is possible to expand the suggested modified system to topologies of microgrids with multiple different energy sources like fuel cells, and diesel generators. This will allow further confirmation of its adaptability, stability, and efficiency in hybrid renewable energy systems.

DOI: 10.46121/pspc.53.4.22

REFERENCES

1. Kumar VV, Kumar BA. Design and Analysis of RBFN Based MPPT Controller for Solar Energy System. In2022 Third International Conference on Intelligent Computing Instrumentation and Control Technologies (ICICICT) 2022 (pp. 843-849). IEEE.
2. Tyagi A, Bihari SP, Chaurasia GS, Choudhury U. MPPT Controller Designed for RBFN-Based Hybrid Energy System. In2023 3rd International Conference on Advancement in Electronics & Communication Engineering (AECE) 2023;1032-1038. IEEE.
3. Rahman A, Farrok O, Haque MM. Environmental impact of renewable energy source based electrical power plants: Solar, wind, hydroelectric, biomass, geothermal, tidal, ocean, and osmotic. Renewable and Sustainable Energy Reviews. 2022;161:112279.
4. Roy P, He J, Zhao T, Singh YV. Recent advances of wind-solar hybrid renewable energy systems for power generation: A review. IEEE Open Journal of the Industrial Electronics Society. 2022;3:81-104.
5. Harrou F, Sun Y, Dairi A, Taghezouit B, Khadraoui S. Advanced data-driven methods for monitoring solar and wind energy systems. Frontiers in Energy Research. 2023;11:1147746.
6. Ceylan C, Devrim Y. Green hydrogen based off-grid and on-grid hybrid energy systems. International Journal of Hydrogen Energy. 2023;48(99):39084-96.
7. Pan T, Wang Z, Tao J, Zhang H. Operating strategy for grid-connected solar-wind-battery hybrid systems using improved grey wolf optimization. Electric Power Systems Research. 2023;220:109346.
8. Hameed AR, Aftan AO, Kudher NA. A structured review of MPPT Techniques For Photovoltaic systems. InAIP Conference Proceedings 2023;2804(1). AIP Publishing.
9. Ahmad M, Numan A, Mahmood D. A comparative study of perturb and observe (P&O) and incremental conductance (INC) PV MPPT techniques at different radiation and temperature conditions. Eng. Technol. J. 2022;40(2):376-85.
10. Yaqoob MT, Rahmat MK, Maharum SM, Su'ud MM. A review on harmonics elimination in real time for cascaded h-bridge multilevel inverter using particle swarm optimization. International Journal of Power Electronics and Drive Systems. 2021;12(1):228-40.
11. Choudhury S, Bajaj M, Dash T, Kamel S, Jurado F. Multilevel inverter: A survey on classical and advanced topologies, control schemes, applications to power system and future prospects. Energies. 2021;14(18):5773.
12. Zhao Z, Wang T, Benbouzid M. A fault-tolerant reconfiguration system based on pilot switch for grid-connected inverters. Microelectronics Reliability. 2022;131:114511.
13. Al-Badrani H, Antar RK, Saleh AA. Modeling of 81-Level Inverter Based on a Novel Control Technique. PrzegladElektrotechniczny. 2022;98(3).
14. Sonia C, Tamilselvi S. A novel power conversion structure for grid-connected photovoltaic applications based on MLI and LeBlanc transformer using IRSA technique. Energy & Environment. 2023:0958305X231210994.
15. Deepika Vinothini T, Karthigaivel R, Barsana banu J. Development of Sliding Mode Control-Adaptive Neuro-Fuzzy Inference Strategy Algorithm for Three-Phase 15-Level MLI. IETE Journal of Research. 2024:1-8.

DOI: 10.46121/pspc.53.4.22

16. Shivakumar P, Barik SK. Implementation of SVM Based Multi-Level Inverter for Grid Connected PV System. Journal Européen des SystèmesAutomatisés. 2022;55(3).
17. Vijayvargiya SP, Sharma VK, Nema P. A novel topology for power quality improvement using EPO incremental conductance MPPT controller for SPV system with 51-level inverter. Electrical Engineering. 2023;105(5):3363-82.
18. Thiyagarajan V. A New 51-Level Asymmetrical Inverter Circuit with Reduced Number of Components. InRecent Advances in Power Electronics and Drives: Select Proceedings of EPREC 2022 2023 (pp. 1-13). Singapore: Springer Nature Singapore.
19. Law KH, Jefry NA, Wong KI. Solar PV based 51-level Hybrid Multilevel Inverter. In2022 IEEE 13th Control and System Graduate Research Colloquium (ICSGRC) 2022 (pp. 83-87). IEEE.
20. Jefry NA, Haw LK, Iing WK. 51-level Multilevel Inverter Configuration for STATCOM Application. In2022 International Conference on Green Energy, Computing and Sustainable Technology (GECOST) 2022 (pp. 129-133). IEEE.
21. Senthilkumar S, Mohan V, Mangaiyarkarasi SP, Karthikeyan M. Analysis of Single-Diode PV Model and Optimized MPPT Model for Different Environmental Conditions. International Transactions on Electrical Energy Systems. 2022;2022(1):4980843.
22. Srinivasan R, Ramalingam Balamurugan C. Deep neural network based MPPT algorithm and PR controller based SMO for grid connected PV system. International Journal of Electronics. 2022;109(4):576-95.
23. Predić B, Jovanovic L, Simic V, Bacanin N, Zivkovic M, Spalevic P, Budimirovic N, Dobrojevic M. Cloud-load forecasting via decomposition-aided attention recurrent neural network tuned by modified particle swarm optimization. Complex & Intelligent Systems. 2024;10(2):2249-69.
24. Trojovský P, Dehghani M. Walrus optimization algorithm: a new bio-inspired metaheuristic algorithm.
25. Prince, Mohammad Kamruzzaman Khan, Mohammad T. Arif, Ameen Gargoom, Aman MT Oo, and Md Enamul Haque. "Modeling, parameter measurement, and control of PMSG-based grid-connected wind energy conversion system." Journal of Modern Power Systems and Clean Energy 9, no. 5 (2021): 1054-1065.
26. Ilten E. Conformable fractional order controller design and optimization for sensorless control of induction motor. COMPEL-The international journal for computation and mathematics in electrical and electronic engineering. 202;41(5):1528-41.
27. Nouh M, Zalam BA, Sayed A. Hybrid FOT2F-FOPD controller for permanent magnet synchronization motor based on ILA optimization with SRF-PLL. Scientific Reports. 2024;14(1):13095.
28. Azizi M, Talatahari S, Gandomi AH. Fire Hawk Optimizer: A novel metaheuristic algorithm. Artificial Intelligence Review. 2023;56(1):287-363.
29. Shishehgarkhaneh MB, Azizi M, Basiri M, Moehler RC. BIM-based resource tradeoff in project scheduling using fire hawk optimizer (FHO). Buildings. 2022;12(9):1472.
30. Nasir M, Suleiman MS, Bansal RC. Control of Master-Slave Microgrid Based on PR and PI Controllers in Islanded Mode. In2022 2nd International Conference on Electronic and Electrical Engineering and Intelligent System (ICE3IS) 2022 (pp. 46-50). IEEE.

DOI: 10.46121/pspc.53.4.22

31. Atar T, Balci S, Kayabasi A. Determination of output current THD of multilevel inverter by ANN. Measurement. 2023;210:112525.
32. Anil G, Murugan N, Ubaid M. PI Controller based MPPT for a PV System. IOSR Journal of Electrical and Electronics Engineering. 2013;6(5):10-5.
33. Rahayu ES, Ma'arif A, Cakan A. Particle swarm optimization (PSO) tuning of PID control on DC motor. International Journal of Robotics and Control Systems. 2022;2(2):435-47.
34. Ashok B, Michael PA. A non-isolated high step-up converter with TID controller for solar photovoltaic integrated with EV. Analog Integrated Circuits and Signal Processing. 2024;118(3):505-21.
35. Mosaad MI. Whale optimization algorithms-based PI controllers of STATCOM for renewable hybrid power system. World journal of modelling and simulation. 2020;16(1):26-40.
36. Yazıcı İ, Yaylacı EK. Modified grey wolf optimizer based MPPT design and experimentally performance evaluations for wind energy systems. Engineering Science and Technology, an International Journal. 2023;46:101520.
37. Al-Samawi, A. A., and H. Trabelsi. New Nine-Level Cascade Multilevel Inverter with a Minimum Number of Switches for PV Systems. Energies 2022, 15, 5857. 2022.
38. Hassan A, Yang X, Chen W. A multi-cell 21-level hybrid multilevel inverter synthesizes a reduced number of components with voltage boosting property. IEEE Access. 2020;8:224439-51.
39. Sarebanzadeh M, Hosseinzadeh MA, Garcia C, Babaei E, Islam S, Rodriguez J. Reduced switch multilevel inverter topologies for renewable energy sources. IEEE Access. 2021;9:120580-95.
40. Ali, Ahmed Ismail M., Zuhair Muhammed Alaas, Mahmoud A. Sayed, Abdulaziz Almalaq, Anouar Farah, and Mohamed A. Mohamed. "An efficient MPPT technique-based single-stage incremental conductance for integrated PV systems considering flyback central-type PV inverter." Sustainability 14, no. 19 (2022): 12105.
41. Alhawsawi, Edrees Yahya. "A Unified Framework for Multi-Level Control and Multi-Objective Optimization of Hybrid Campus Microgrids: Integrating Adaptive MPC, Modified Firefly Algorithm, and Homer Simulations." PhD diss., Oakland University, 2024.
42. Jin, Tao, Jintao Guo, Mohamed A. Mohamed, and Mengqi Wang. "A novel model predictive control via optimized vector selection method for common-mode voltage reduction of three-phase inverters." IEEE Access 7 (2019): 95351-95363.
43. Rao, Chaoping, Ali Hajjiah, Mohammed A. El-Meligy, Mohamed Sharaf, Ahmed T. Soliman, and Mohamed A. Mohamed. "A novel high-gain soft-switching DC-DC converter with improved P&O MPPT for photovoltaic applications." IEEE access 9 (2021): 58790-58806.
-to-make-driving-safer-and/}.

DOI: 10.46121/pspc.53.4.22